

The ZTF-BTS Type Ia supernovae luminosity function suggests a single progenitor channel for the explosions

Amir Sharon¹[★] and Doron Kushnir¹

¹*Dept. of Particle Phys. & Astrophys., Weizmann Institute of Science, Rehovot 76100, Israel*

Accepted XXX. Received YYY; in original form ZZZ

ABSTRACT

We construct the Type Ia supernovae (SNe Ia) luminosity function (LF) using the ZTF Bright Transient Survey (BTS) catalogue. While this magnitude-limited survey has an unprecedented number of objects, it suffers from large distance uncertainties and lacks an estimation of host extinction. We bypass these issues by calculating the intrinsic luminosities from the shape parameters of the light curve's g and r bands, with the luminosities calibrated from the well observed SNe Ia sample of the Carnegie Supernova Project, allowing us to construct, for the first time, the intrinsic LF of SNe Ia. We then use a novel tight relation between the color stretch and the synthesized ^{56}Ni mass, $M_{\text{Ni}56}$, to determine the $M_{\text{Ni}56}$ distribution of SNe Ia. We find that the LFs are unimodal, with their peaks in line with previous results, but have a much lower rate of dim events and luminous events. We show that the features on top of the unimodal LF-derived distributions are all consistent with statistical noise, suggesting a single progenitor channel for the explosions. We further derive, for the first time, the SNe Ia distribution of host galaxy extinction, and find a mean selective extinction of $E(B - V) \approx 0.1$ and a non-negligible fraction with large, > 1 mag, extinction in the optical bands. The high extinction is typical for luminous SNe, supporting their young population origin.

Key words: supernovae: general - methods: data analysis - surveys

1 INTRODUCTION

Type Ia supernovae (SNe Ia) are widely accepted to be the result of thermonuclear explosions of white dwarfs (WDs), but their progenitor systems and explosion mechanism are still under debate (for a review, see, e.g., Maoz et al. 2014). The luminosities of SNe Ia, powered by the radioactive decay chain of ^{56}Ni , span a significant range (Phillips 1993). The peak bolometric luminosities vary between $10^{42} - 10^{43} \text{ erg s}^{-1}$ and the synthesized ^{56}Ni masses, $M_{\text{Ni}56}$, vary between $\sim 0.1 - 1 M_{\odot}$ (see Sharon & Kushnir 2020b, for a recent compilation).

There is an ongoing debate in the literature on whether the observed range of SNe Ia properties can be explained by a single progenitor channel or whether multi-progenitor channels are required. The latter was favoured in Pakmor et al. (2013), supported by the bimodal distribution of the B band magnitude decline during the first 15 days after the peak, $\Delta m_{15}(B)$, taken from the CfA3 sample (Hicken et al. 2009). Subsequent works that analysed the $\Delta m_{15}(B)$ distribution have repeated this claim (Ashall et al. 2016; Hakobyan et al. 2020). However, the $\Delta m_{15}(B)$ bi-modality is driven by a clustering of low-luminosity SNe Ia in a small range of $\Delta m_{15}(B)$, where the peak luminosity is not a monotonic function of $\Delta m_{15}(B)$ (Burns et al. 2018), questioning the reality of the bi-

modal distribution. Multiple explosion channels are also favoured by Polin et al. (2019), which divided the population of SNe Ia using the Si II velocity and the peak magnitude. Other lines of evidence suggest a single progenitor channel. These include the continuous and relatively uniform properties of SNe Ia, which would require a fine tuning of the multi-progenitor channels (Maoz et al. 2014). This perspective has been recently highlighted by the tight correlation of $M_{\text{Ni}56}$ with the γ -ray escape time, t_0 (Wygoda et al. 2019; Sharon & Kushnir 2020a).

An accurately measured SNe Ia luminosity function (LF), which describes the intrinsic luminosity distribution of these SNe, can constrain the progenitor systems. For example, consider the case of two progenitor channels with significant rates but different intrinsic LFs. In this case, the total LF will show some structure where the two channels overlap (if the two channels do not overlap, the LF would not be unimodal). However, in order to obtain the intrinsic LF, the host galaxy's extinction must be taken into account, which usually cannot be easily done. Instead, many surveys in the last decades obtained a pseudo LF (PLF), in which the host galaxy's extinction is not removed. While the PLF is useful on its own for many applications, the relation to the intrinsic LF is not clear. In fact, we show in this work that there is a significant difference between the PLF and the intrinsic LF of SNe Ia. This is because a host extinction in optical wavelengths is typically a few tenths of a magnitude and can be larger than 1 mag (Phillips et al. 2013, see also Section 9).

[★] E-mail: amir.sharon@weizmann.ac.il

The difference between the PLF and the LF complicates comparison of the predictions of various (extinction-free) models with the observations (see, e.g., [Ruiter et al. 2013](#); [Shen et al. 2017](#)).

A prime example of a survey that aimed to construct the PLF out of a complete volume-limited sample of SNe is the Lick Observatory Supernova Search (LOSS; [Leaman et al. 2011](#); [Li et al. 2011a,b](#); [Maoz et al. 2011](#)). The SNe Ia sample consists of 74 SNe discovered between 1998–2006, all with associated host galaxies within a distance of 80 Mpc. Using the known distances to the galaxies, an absolute peak magnitude PLF within the range $\approx [-16.7, -19.5]$ mag (of a filter that most closely matches the R band) was constructed. Subsequent works have analysed the host galaxies’ properties ([Graur et al. 2017a,b](#)), re-examined the SNe classifications ([Shivvers et al. 2017](#)), and constructed the M_{Ni56} distribution ([Piro et al. 2014](#)).

More recent surveys are also useful for constraining the LF. The CN1a0.02 ([Chen et al. 2020](#)) is a volume-limited survey of nearby SNe with $z < 0.02$ discovered by the All-Sky Automated Survey for Supernovae (ASAS-SN; [Kochanek et al. 2017](#)), with 240 SNe Ia. The survey is complete for SNe with a V band peak magnitude of $m_V < 16.5$ mag, which corresponds to absolute magnitudes of $M_V \lesssim -18.2$ mag at $z = 0.02$. Since the dimmest SNe Ia peak magnitudes reach ≈ -17 mag ([Taubenberger 2017](#); [Burns et al. 2018](#)), and extinction further increases the observed magnitudes, a volume correction would be required for the low-luminosity end of the LF.

The Zwicky Transient Facility (ZTF) Bright Transient Survey (BTS; [Fremming et al. 2020](#); [Perley et al. 2020](#), hereafter P20) seeks to identify and classify extragalactic transients in the Northern sky. The objects are observed in the g and r bands and are spectroscopically classified. The number of objects substantially increased compared to previous surveys, with over a thousand of identified SNe per year, most of them SNe Ia. If available, the redshift of the transient is determined from the host galaxy, or otherwise from the SN spectral features. In practice, a significant fraction of SNe lack a spectroscopic redshift of the host. In P20, the SNe with an observed peak magnitude of $m < 18.5$ mag are used to construct the PLF and measure the total rate of each SNe type. They found for SNe Ia an absolute peak magnitude range of $\approx [-16.5, -20.5]$ mag and a total rate of $\approx 2.35 \times 10^4 \text{ Gpc}^{-3} \text{ yr}^{-1}$.

Another well known SNe survey is the Carnegie Supernova Project (CSP; [Contreras et al. 2010](#); [Stritzinger et al. 2011](#); [Krisciunas et al. 2017](#); [Burns et al. 2018](#), and others). The CSP’s Ia sample consists of 123 well observed SNe Ia, with independent distance estimates. The high cadence of observations over a large range of wavelengths enables the estimation of the total extinction using templates ([Burns et al. 2018](#)), and also the construction of the bolometric luminosity ([Scalzo et al. 2019](#); [Sharon & Kushnir 2020b](#)). However, the sample is not complete and cannot be used to study SNe rates.

In this work, we use a combination of the BTS public catalogue¹ and the CSP Ia sample to accurately determine the LF of SNe Ia. We first compare in Section 2 the light curve shapes of the CSP and the BTS samples to show that the host extinction and the distance uncertainties significantly affect the luminosity distribution. In order to partly bypass these difficulties, we use the tight correlations between the light curve color stretch, s_{gr} ([Ashall et al. 2020](#)) and the intrinsic luminosity, as calibrated from the CSP Ia sample. The use of s_{gr} allows the accurate determination of the

intrinsic luminosity for the entire luminosity range of SNe Ia (this is a variant of s_{BV} , introduced by [Burns et al. 2014, 2018](#)). We determine s_{gr} values for the vast majority of the BTS survey in Section 3. In Section 4, we estimate the SNe distances (for the ones that lack a spectroscopic redshift of the host) and investigate the completeness of the sample. We find that most of the sample is complete up to ~ 180 Mpc, and we use this distance to construct a volume-limited sub-sample that is used for our main results. In Section 5, we construct, for the first time, the intrinsic s_{gr} distribution (upper panel of Figure 1) and the LF (Figure 2). We find that the rate of dim events is lower by almost an order of magnitude than the corresponding PLF values of P20, and that the dimmest event has a peak magnitude of $M_r \approx -17.5$ mag, much more luminous than the dimmest PLF events of P20 with $M_r \approx -16.7$ mag. We find a total rate of $\approx 2.91^{+0.58}_{-0.45} \text{ Gpc}^{-3} \text{ yr}^{-1}$ (per comoving element in the redshift range $z \approx [0.01, 0.04]$), consistent with previous studies ([Dilday et al. 2010](#); [Graur et al. 2011](#); [Li et al. 2011b](#); [Frohmaier et al. 2019](#); [Perley et al. 2020](#)).

We then use in Section 6 the CSP Ia sample to calibrate a novel tight relation between s_{gr} and M_{Ni56} (middle panel of Figure 1). M_{Ni56} is determined using the methods of [Sharon & Kushnir \(2020b\)](#), which use the bolometric light-curve and require accurate distances and measurements over long periods of time and over a wide range of wavelengths. While these requirements are fulfilled for many SNe in the CSP sample, they are difficult to achieve in a complete survey with thousands of objects per year, such as the ZTF BTS. Combining the $M_{\text{Ni56}}-s_{gr}$ relation with the s_{gr} distribution allows us to determine the M_{Ni56} distribution, which is the main result of this paper (bottom panel of Figure 1, blue symbols). In Appendix A, we also apply our methods to the LOSS sample to determine the M_{Ni56} distribution (green symbols). For comparison, the results of [Piro et al. \(2014\)](#), based on the LOSS sample, are shown as red symbols.

We find that the LF, the s_{gr} , and the M_{Ni56} distributions are unimodal. The peaks of the distributions are at $M_r \approx -19.2$ and $M_{\text{Ni56}} \approx 0.6 M_{\odot}$ (in agreement with P20 and [Piro et al. 2014](#), respectively). The rates of dim events ($M_{\text{Ni56}} \lesssim 0.4 M_{\odot}$) and luminous events ($M_{\text{Ni56}} \gtrsim 0.8 M_{\odot}$) are lower by at least a factor of 5 from the rate of the most common, $M_{\text{Ni56}} \approx 0.6 M_{\odot}$, events. We perform Monte Carlo (MC) simulations to show that the features on top of the unimodal-derived distributions are all consistent with statistical noise (Section 7). The derived distributions, therefore, suggest a single progenitor channel for the explosions.

We construct similar distributions for different host properties in Section 8. We show that the BTS LF of SNe Ia in early-type galaxies is more inclined towards low-luminosity events than the LF of SNe Ia in star-forming galaxies (similar to the results of [Li et al. 2011a](#); [Ashall et al. 2016](#)). In Section 9, we construct, for the first time, the distribution of the host galaxy extinction for a subsample of the BTS with accurate distances and for the LOSS survey. We find a mean $E(g-r)$ value of ~ 0.1 mag, and that a non-negligible fraction of SNe, especially in star-forming galaxies, exhibit large extinction values, $\gtrsim 1$ mag, in the optical bands. We find that a host galaxy extinction, A^h , is highly correlated with the luminosity of the SNe. For example, in the r band, luminous SNe with $s_{gr} \gtrsim 1$ suffers from $A^h \approx 1$ mag for a non-negligible fraction of the SNe. We found no low s_{gr} SNe with A^h larger than 1 mag. These results are in line with the idea that luminous SNe Ia originate from young populations, while low-luminosity SNe Ia require old progenitors. We summarise our results in Section 10, highlighting the importance of acquiring spectroscopic redshift for all SNe hosts, which would tightly constrain the intrinsic LF.

¹ <https://sites.astro.caltech.edu/ztf/bts/explorer.php>, downloaded on July 2021, with 1519 SNe Ia that passed the quality cuts described in P20.

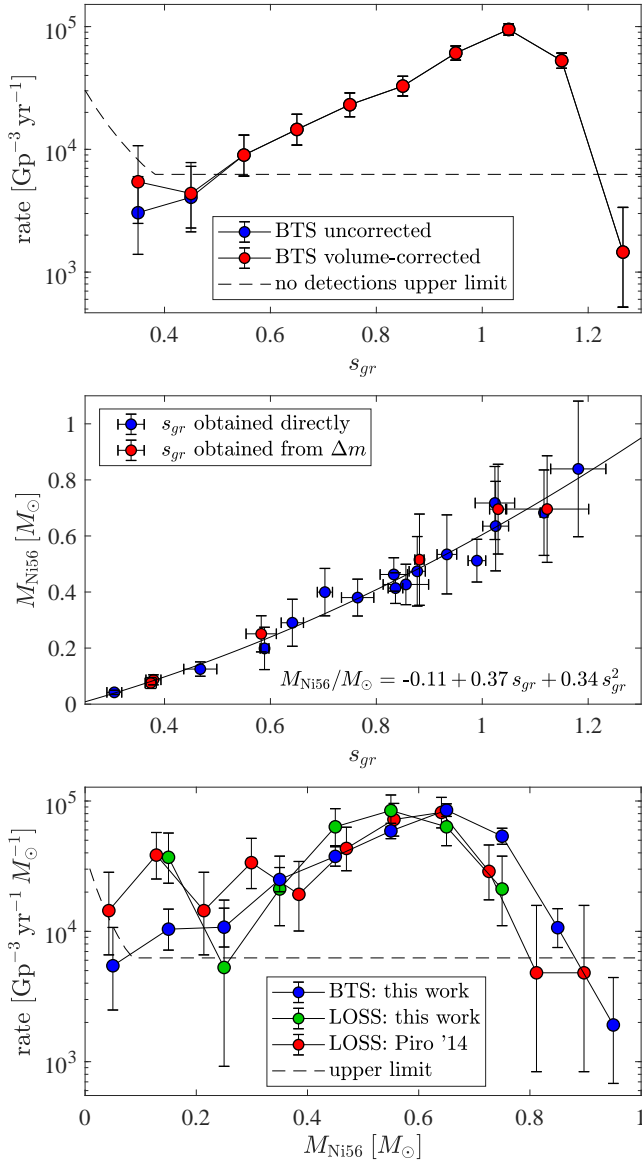


Figure 1. The main results of the paper. Top panel: The s_{gr} distribution of the 180 Mpc volume-limited BTS sample. Volume-uncorrected (-corrected) results are shown as blue (red) symbols, with the volume-uncorrected rates scaled to match the total volume-corrected rate (only the dimmest bin, with three SNe, requires a non-negligible volume correction). The black, dashed line indicates the 95 per cent upper limit for no detections in a bin of 0.1. Middle panel: The M_{Ni56} - s_{gr} distribution of the CSP sample. Blue symbols indicate SNe Ia with a direct s_{gr} measurement, while red symbols indicate SNe Ia with s_{gr} obtained through a decline-rate relation. Bottom panel: The M_{Ni56} distribution from BTS (this work, blue), LOSS (this work, green), and of Piro et al. (2014) (red). The black, dashed line indicates the 95 per cent upper limit for no detections in a bin of $0.1 M_{\odot}$.

In Appendix A, we elaborate on our analysis of the LOSS sample. In Appendix B, we analyse the effects of the SNe redshift distribution and the filter transmission functions on the decline rates and peak magnitudes. In Appendix C, we describe a few different methods to calculate the LF and we compare between volume-limited LF and magnitude-limited LF. In Appendix D, we provide the properties of each SNe Ia from the BTS, CSP, and LOSS samples that are used in this work. The provided data can be used to reproduce the main results of this paper.

2 BTS-CSP COMPARISON

In this section, we analyse the PLF derived in P20 by comparing the BTS light curves to the CSP sample. The ZTF BTS public catalogue (Fremling et al. 2020, P20) includes, for each transient, the light curves in the g and r bands, the observed peak magnitude, the galactic extinction in the direction of the transient and the redshift. The provided absolute peak magnitude is inferred from the observed peak magnitude, Galactic extinction, and the distance (determined from the redshift through a cosmological model with $\Omega_M = 0.3$, $\Omega_{\Lambda} = 0.7$ and $h = 0.7$). Fremling et al. (2020) reported that about 44 per cent of the objects were associated with host galaxies that have a catalogued spectroscopic redshift, which was obtained by searching for galaxies within $2'$ of the SN. For the other cases, the redshift is determined from the SN spectral features, with a non-negligible uncertainty of $\Delta z \approx 0.005$ (Fremling et al. 2020, P20). For construction of the PLF the host extinction is not required (note, however, that in optical wavelengths the host extinction is typically a few tenths of a magnitude and can be larger than 1 mag; Phillips et al. 2013, see also Sections 4 and 9).

In this work, using the NASA Extragalactic Database (NED)² and the Sloan Digital Sky Survey (SDSS)³ catalogues, we obtained the spectroscopic redshift of ≈ 35 per cent of the SNe. This was achieved by using the methods described in Ofek (2014) and Soumagnac & Ofek (2018), and a search radius of 10 kpc around the SN location. The angular size of the search radius was estimated with the provided redshift.

To build the PLF and to calculate the SNe rate, the authors of P20 only considered objects with observed peak magnitudes brighter than $m_{lim} = 18.5$ mag. They considered several completeness factors and calculated the volumetric rate by:

$$R = \frac{1}{T} \frac{1}{f_{global}} \sum_{i=1}^N w_i, \quad (1)$$

where $T = 2.12$ yr and $N = 875$ are, respectively, the time and number of SNe Ia of the survey, $f_{global} = 0.172$ is the fraction of observed SNe due to the sky coverage, galactic extinction effects and recovery fraction, and w_i are the weights of each SN. The weights are given by $w_i = (f_{cl,i} V_{max,i})^{-1}$, where $f_{cl,i}$ is the classification efficiency that depends on the observed magnitude ($15 \text{ mag} < m < 18.5 \text{ mag}$), and $V_{max,i}$ is the volume within each SN can be detected, given the limiting magnitude:

$$V_{max,i} = \frac{4\pi}{3} \left(10^{\frac{m_{lim} - M_i}{5}} - 8 \right)^3 \text{ Gpc}^3, \quad (2)$$

where M_i is the absolute peak magnitude of the SN. P20 obtained a SNe Ia magnitude range of $[-16.7, -20.66]$ mag (in this method, the dimmest events could be the result of large host extinction). Their PLF, shown in Figure 2, peaks at $m \approx -19$ mag, and the total rate is $(2.35 \pm 0.24) \times 10^4 \text{ Gpc}^{-3} \text{ yr}^{-1}$.

The luminous and the dim ends of the P20 PLF demonstrate the effects of host extinction and distance uncertainties. The highest reported peak magnitude of the sample is $M = -20.66$ mag, which is ~ 1 mag higher than the highest peak magnitude in the CSP sample. Given that the highest peak bolometric luminosity of the CSP sample is $\sim 1.6 \times 10^{43} \text{ erg s}^{-1}$ (Sharon & Kushnir 2020b), and assuming that the rest of the SED is also scaled by the same amount, we obtain a peak luminosity of $\sim 4 \times 10^{43} \text{ erg s}^{-1}$, and a $M_{Ni56} \approx$

² <https://ned.ipac.caltech.edu/>

³ <https://www.sdss.org/>

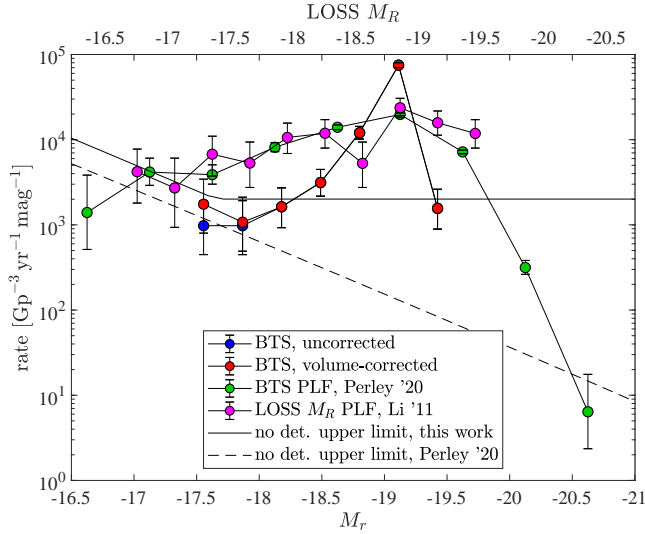


Figure 2. The M_r LF. The BTS volume-corrected (-uncorrected) LF of this work is indicated by red (blue) symbols (only the dimmest bin requires a volume correction). The PLF of P20 and of LOSS (Li et al. 2011a) are indicated by green and magenta symbols, respectively. All the LFs are scaled so that their total rate matches the total BTS volume-corrected rate. The solid (dashed) black lines indicate the 95 per cent upper limit for no detections in a bin of 0.33 (0.5) mag in our (P20) analysis.

$2 M_{\odot}$ for the most luminous reported event. There are also ~ 20 SNe with $M \lesssim -20$ mag (see examples in Table 1), corresponding to $M_{\text{Ni56}} \gtrsim 1.2 M_{\odot}$. We argue below that the luminosity of these objects is, in fact, much lower. We next compare in Figure 3 the g and r absolute magnitude light curves of some of the dimmest SNe of P20 with the CSP sample. The absolute magnitude light curves of the BTS sample were constructed by simply adding the differences between the given absolute and observed peak magnitudes to the observed light curves. For the CSP sample, we use the provided distances and extinction values. As can be seen in the figure, some SNe from the BTS sample display features that are absent in low-luminosity SNe of the CSP sample, such as a shoulder in the r band after the peak or a much slower decline of the g band, and are therefore more likely to be more luminous events. We list in Table 1 the absolute peak magnitudes of these dim SNe, as well as those of the most luminous SNe in the sample. For a reference, we provide the s_{gr} and peak magnitudes of these events from the calibration of Section 3, demonstrating the large differences between our and the P20 calculations. None of the objects in Table 1 have a spectroscopic redshift in our analysis.

In order to quantify the tension between the luminosities and the light-curve shapes, we use the well-known correlation between them (Phillips 1993). While historically the magnitude decline, Δm_{15} , at a given band was used to calibrate the peak magnitude, Burns et al. (2014, 2018) showed that the color stretch parameter, s_{BV} , provides a much better correlation, specifically for low-luminosity SNe Ia. The parameter s_{BV} is obtained by measuring the time difference between the B band peak time and the $B - V$ color peak time:

$$s_{BV} = \frac{t_{\text{max}, B-V} - t_{\text{max}, B}}{30 \text{ day}}. \quad (3)$$

While originally defined in the Johnson photometric system, an equivalent useful parameter, s_{gr} , can be defined for the Sloan filters, with the g and r bands replacing the B and V bands, respectively (Ashall et al. 2020).

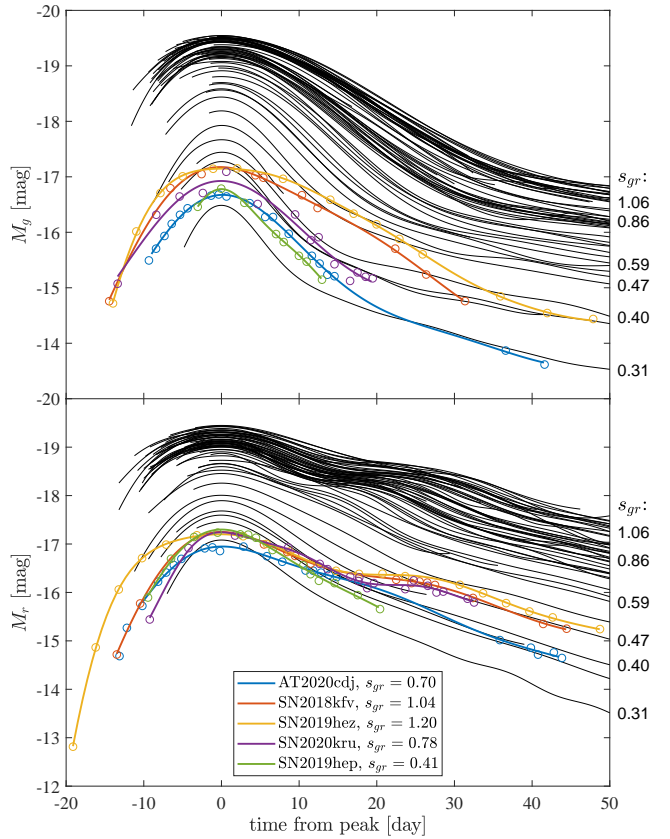


Figure 3. CSP g - and r -band light curves and several BTS SNe with low absolute magnitudes, as determined by P20. The s_{gr} of the BTS SNe is given in the legend, and the s_{gr} of several representing SNe from the CSP are displayed to the right of the figure. The range of the s_{gr} of the BTS sample is between $\approx 0.4 - 1.2$, while the s_{gr} of the CSP SNe for the same luminosities reaches a maximum of ≈ 0.4 .

Table 1. Five of the dimmest and most luminous SNe Ia, as given by the BTS explorer, and are a part of the P20 LF. The absolute magnitudes of these SNe, as calculated from s_{gr} , are in tension with the absolute magnitudes reported by P20. None of these SNe have a spectroscopic redshift.

SN	M_{peak}^a	$M_{\text{peak}}^{s_{gr} b}$	s_{gr}
2020cdj	-16.98	-18.76	0.70
2018kfv	-17.01	-19.18	1.04
2019hez	-17.21	-19.27	1.20
2020kru	-17.24	-18.91	0.78
2019hep	-17.32	-17.81	0.41
2020fxm	-20.21	-19.27	0.88
2019fck	-20.30	-19.46	1.13
2019tmp	-20.30	-19.59	1.26
2020yjf	-20.48	-19.52	1.14
2019phj	-20.66	-19.48	1.14

^a Absolute magnitude of the BTS explorer, calculated from the redshift.

^b Absolute magnitude of this work, calculated from s_{gr} .

We downloaded the sample of BTS objects after 3.13 years of observations; it consists of 1519 SNe Ia (note that only a sub-sample is used to construct the LF, see Appendix C). We obtained the spectroscopic redshifts of 528 SNe with the use of the NED and SDSS catalogues. We measure the light curves' properties (and estimated the errors of the derived values) by using Gaussian processes interpolations as implemented by the SNooPy package (Burns et al.

Table 2. Properties of the fits to the peak magnitudes with respect to $\ln(s_{gr})$ for the SNe in the CSP sample.

parameter	fit variable	p_0^a	p_1^a	p_2^a	N^b	scatter
M_g	$\ln(s_{gr})$	-19.37	-1.01	1.18	37	0.06
M_r	$\ln(s_{gr})$	-19.22	-0.81	0.80	37	0.08
M_B	$\ln(s_{gr})$	-19.40	-0.98	1.91	32	0.11
M_V	$\ln(s_{gr})$	-19.30	-0.88	1.25	31	0.10

^a Polynomial coefficient to the equation $p_0 + p_1 x + p_2 x^2$ ^b Number of objects used to determine the fit

2011). The results of the CSP and BTS samples are given in Tables D1 and D3, respectively (see Section 3 for details). The peak magnitude- s_{gr} distributions of the CSP and the BTS samples are shown in Figure 4. In this plot, the peak magnitudes of both samples are calculated from the observed magnitudes, the provided distance, and the galactic extinction. We further correct for the host extinction of the CSP sample and apply a K -correction for both the CSP and the BTS samples (which somewhat differs from the K -correction of P20, see Appendix B for details).

As can be seen in Figure 4, the peak magnitudes are tightly correlated with s_{gr} for the CSP sample, with a sharp decrease in luminosity as s_{gr} decreases. To characterize this relation, we fit the peak magnitudes to a second-degree polynomial in $\ln(s_{gr})$ and obtained a scatter of ≈ 0.06 (0.08) mag in the g (r) band. The fit parameters are given in Table 2. Since the scatter of the fits is dominated by an intrinsic scatter that is much larger than the typical error, the χ^2 values of the fits are very large and are not shown. The scatter of the BTS peak magnitudes with similar s_{gr} values is significantly larger. Figure 5 shows the deviations between the BTS absolute magnitude, M^z , calculated with the estimated redshifts and neglecting host extinction, and the absolute magnitude predicted by the CSP fit at the measured s_{gr} , $M^{s_{gr}}$. SNe with spectroscopic redshifts are indicated by the grey bars while the whole sample is indicated by the red lines. To accurately compare the absolute magnitudes between the surveys, we applied corrections to the CSP results, taking into account the different filter transmission functions (see Appendix B for details). As can be seen in Figure 5, the magnitude differences have a bias of $\approx 0.3 - 0.4$ mag in the g band and $\approx 0.15 - 0.25$ in the r band, which is most likely the results of ignoring the host extinction. For the whole sample, a non-negligible fraction of SNe have unphysical negative values, which is less frequent for SNe with spectroscopic redshifts, suggesting they are the result of distance errors.

3 DETERMINATION OF THE COLOUR STRETCH PARAMETER

We next sought to apply the CSP peak magnitude- s_{gr} relation to the BTS sample. However, we were able to directly determine s_{gr} values for only 204 out of the available 1519 SNe. The reason is that a determination of s_{gr} requires measurements of both bands for at least ~ 30 days, which is the typical time between the g -band-peak and the color maximum, and such late observations are not always available. Also, for many SNe, the g -band-peak time cannot be determined, since there are no pre-peak observations. It is also possible that poor sampling does not allow the determination of neither of the two times. To overcome this issue, we measure several decline rate parameters, which are easier to determine, and attempt to find correlations between them and s_{gr} , in order to recover s_{gr} from these decline rate parameters. We consider $\Delta m_{15}(g)$, $\Delta m_{15}(r)$,

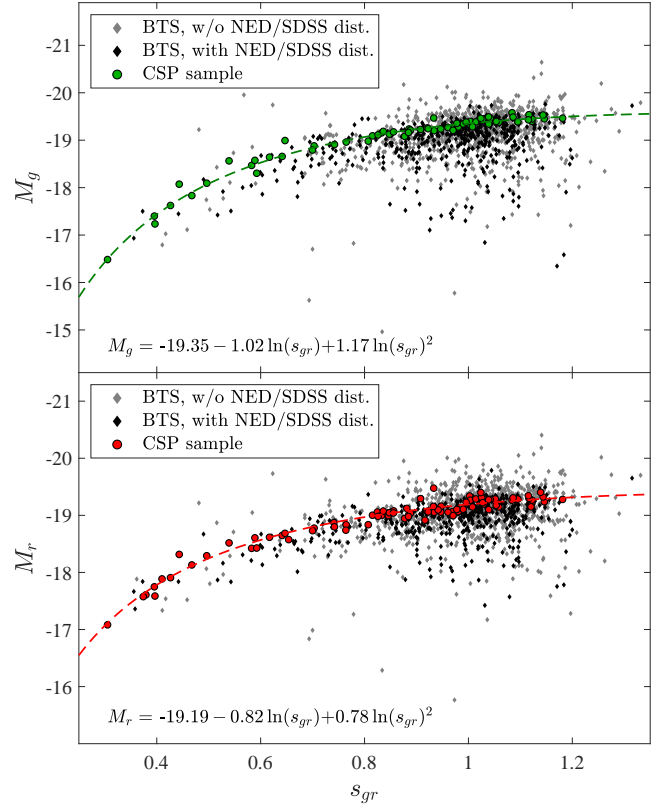


Figure 4. s_{gr} –peak magnitude distribution of the CSP sample and of the BTS sample (using the redshift for the BTS sample). Upper panel: g -band absolute magnitude as a function of s_{gr} . The CSP values are indicated by green circles, and the BTS values by black (grey) diamonds for SNe with (without) a spectroscopic redshift. The fit to the CSP sample is indicated by a dashed line and is displayed in the bottom of the panel. Bottom panel: Same as the top panel but for the r band with red symbols.

$\Delta m_8(g)$, and $\Delta m_{30}(r)$, which measure the magnitude difference at the specified number of days from the peak magnitude of the band.

Using SNe with both s_{gr} and some Δm parameter measured, we fit s_{gr} as a first- or second-order polynomial in Δm :

$$s_{gr} = p_0 + p_1 \Delta m + p_2 (\Delta m)^2, \quad (4)$$

where p_i are the fit parameters ($p_2 = 0$ is zero for first-order polynomials). The fit to $\Delta m_8(g)$ is divided into two linear fits. We make separate fits for the CSP and BTS samples, due to the differences between the redshift distribution and the filter response functions of the two surveys (see discussion below). Figure 6 shows the distribution of s_{gr} and the decline rate parameters of both samples. BTS SNe with both s_{gr} and decline rate measurements are shown as blue circles, with the fit to the results denoted by a black, solid line. Since the color stretch can often be determined from several decline rate parameters, and in order to check for consistency, for each panel, we also plot the s_{gr} values that were determined using a different decline rate parameter (red circles). CSP SNe are indicated by green diamonds, with the fit to the results in a black, dashed line. A similar plot that includes only the CSP results is given in Appendix D; there, the error bar of each measurement is indicated, and the SNe with both s_{gr} and decline rate measurements are presented separately from the SNe for which the s_{gr} values were determined using a different decline rate parameter. The parameters of the fits in each s_{gr} range are given in Table 3.

The differences between the BTS and the CSP relations are

Table 3. The CSP and ZTF decline rates as a function of s_{gr} fit parameters, used in Equation (4). For each fit, only SNe within the indicated s_{gr} range were part of the fit. The BTS $\Delta m_8(g)$ fit for low s_{gr} values uses both BTS and CSP SNe.

	decline rate	s_{gr} range	p_0	p_1	p_2	N^a	χ^2/dof	scatter
CSP	$\Delta m_{15}(g)$	$s_{gr} > 0.5$	1.47	-0.53	-	29	3.37	0.035
	$\Delta m_{15}(r)$	$s_{gr} < 0.7$	0.93	-0.42	-	10	2.70	0.021
	$\Delta m_8(g)$	$s_{gr} > 0.65$	1.41	-1.37	-	27	2.70	0.037
	$\Delta m_8(g)$	$s_{gr} < 0.65$	1.01	-0.62	-	10	1.34	0.016
	$\Delta m_{30}(r)$	-	1.41	-0.16	-0.13	35	4.37	0.036
BTS	$\Delta m_{15}(g)$	$s_{gr} > 0.5$	1.61	-0.59	-	192	1.83	0.050
	$\Delta m_8(g)$	$s_{gr} > 0.65$	1.46	-1.20	-	198	2.44	0.056
	$\Delta m_8(g)$	$s_{gr} < 0.65$	1.15	-0.78	-	9	0.95	0.025
	$\Delta m_{30}(r)$	-	1.37	-0.13	-0.13	202	1.09	0.051

^a Number of objects used to determine the fit

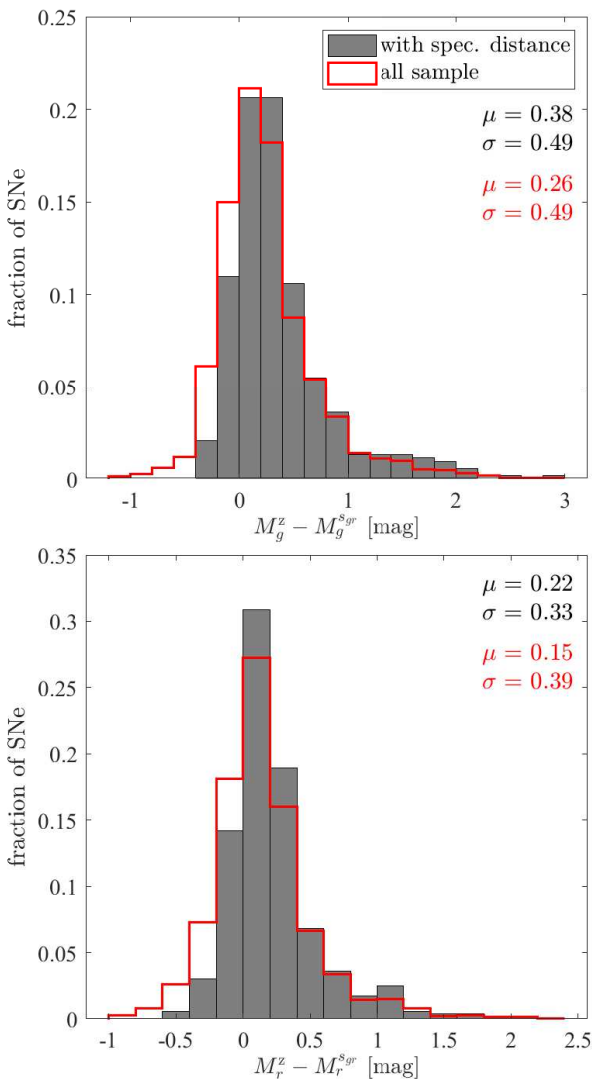


Figure 5. Distributions of the differences between the absolute magnitudes calculated with the redshift estimate, M^z , and the absolute magnitudes calculated with s_{gr} , M^{sgr} . The distributions of the SNe with spectroscopic redshifts are indicated by grey-filled bars, and the whole sample by red lines. Top (bottom) panel: the g (r) band distributions. The distributions have a bias of $\approx 0.3 - 0.4$ mag and $\approx 0.15 - 0.25$ in the g and r band, respectively.

studied in detail in Appendix B with synthetic photometry of SNe Ia spectra. We find that the mean g -band decline rates are larger when the BTS parameters are used, while they hardly change for the r band. This is in quantitative agreement with the differences seen in the g band and with the similarity in the r band between the two samples shown in Figure 6.

Ideally, we would like to determine s_{gr} solely from the relations derived from the BTS data. However, the range of decline rate values with an observed s_{gr} is not entirely covered. Specifically, there is only one SNe with $\Delta m_{15}(r) > 1$, three SNe with $\Delta m_8(g) > 0.7$ and no SNe with $\Delta m_{30}(r) > 2$ that have an observed s_{gr} , so it is not possible to determine a fit for these regimes from the BTS data alone. We are, therefore, forced to use the CSP fits in these regions⁴. We expect this procedure to have a minimal effect, since $\Delta m_8(g)$ and the r -band decline rates are hardly affected by the redshift and the different filter transmission functions (see Figure B1).

The validity ranges of the fits are determined by requiring the decline rate to provide a good estimate for s_{gr} (these ranges sometimes do not span the entire s_{gr} range over which the fit is determined). The s_{gr} scatter of the CSP fits is lower than $\Delta s_{gr} < 0.04$, and the reduced χ^2 values are higher than 2.5 for all fits except one, indicating that the scatter is most probably caused by the intrinsic scatter of the decline rate-color stretch relation. Due to the larger uncertainty in the shape parameters of the BTS sample, the scatter of the BTS fits is higher, and the reduced χ^2 values are lower, $\sim 1 - 2$. This indicates that for the BTS fits the scatter could be either due to the uncertainty of the shape parameters (for $\chi^2 \approx 1$) or due to an intrinsic scatter (for $\chi^2 > 1$).

Using the four decline rate parameters, we were able to determine the s_{gr} for another 1167 SNe from the BTS sample. This was done in the following order. First, 8 SNe with $\Delta m_{15}(r) > 1$ were fitted using $\Delta m_{15}(r)$. Then, due to its low scatter compared with the other decline rates, $\Delta m_{15}(g)$ was used to fit another 853 SNe. 208 SNe with no $\Delta m_{15}(g)$ measurement or with high $\Delta m_{15}(g)$ values were fitted from $\Delta m_8(g)$, and lastly, 98 SNe were fitted from $\Delta m_{30}(r)$. 16 SNe have less than five observed epochs in both bands and are not considered in our analysis. An additional 89 SNe have $\Delta m_{15}(r) < 1$ and no other decline rate measurement, so their s_{gr} value cannot be accurately estimated, but they are ruled out as being very dim, and therefore would not change the estimated LF significantly. For 30 SNe, we were unable to identify a peak magnitude in either band. This leaves 13 SN with an observed peak but

⁴ We use both BTS and CSP SNe for the $\Delta m_8(g)$ fit at low, < 0.7 , s_{gr} values, and the CSP SNe with $\Delta m_{30}(r) > 2$ for the $\Delta m_{30}(r)$ fit.

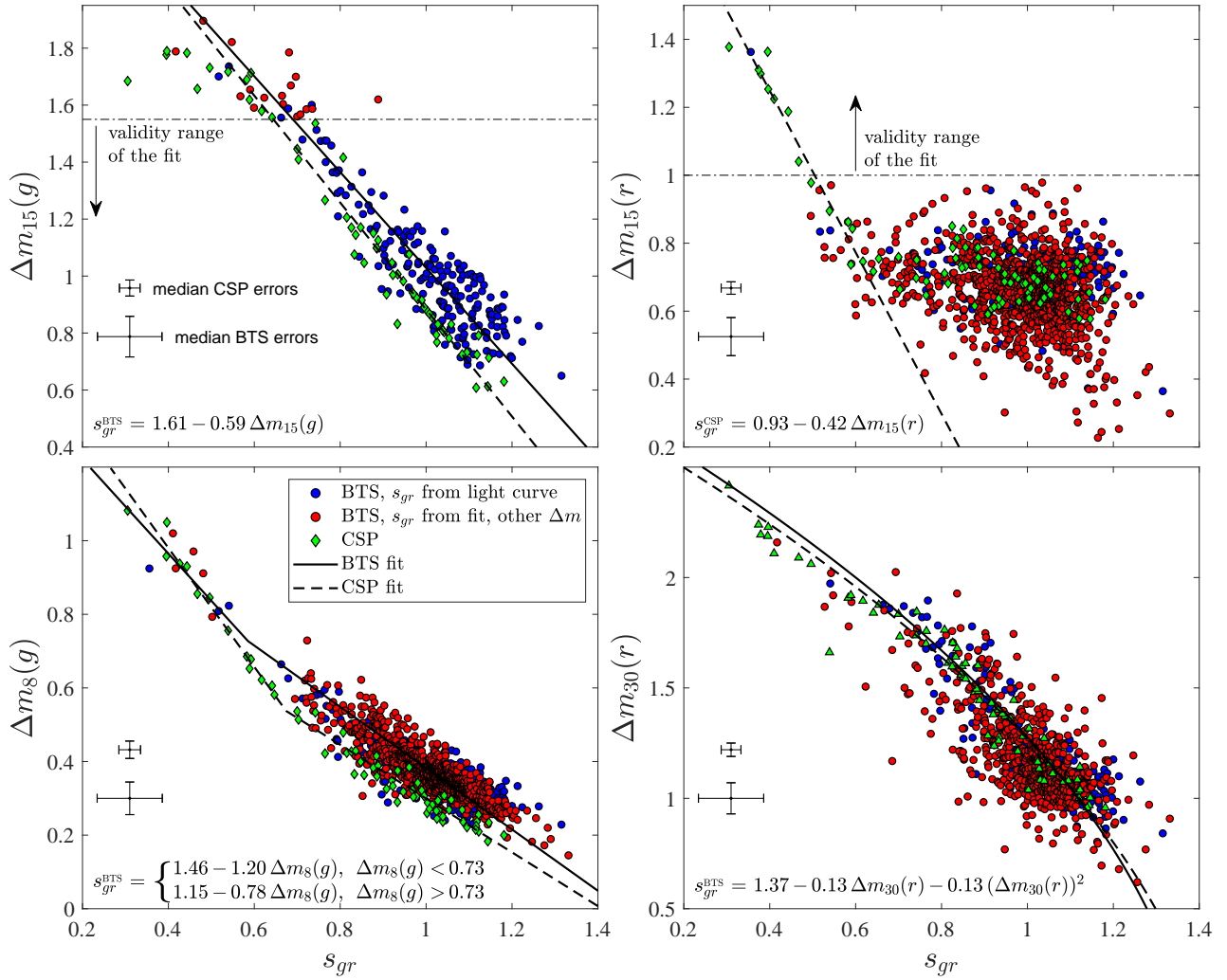


Figure 6. Decline rate parameters as a function of s_{gr} . BTS SNe with a direct s_{gr} measurement are shown in blue circles. BTS SNe whose s_{gr} is determined using a different decline rate parameter are shown in red circles. CSP SNe are marked by green diamonds. The median errors of the two samples are indicated in each plot. Fits of the BTS and CSP samples results are shown in black, solid lines and black, dashed lines, respectively. Also shown are the validity ranges of the $\Delta m_{15}(g)$ and $\Delta m_{15}(r)$ fits. SNe whose decline rate is outside the validity range are not fitted with a s_{gr} value from that decline rate.

no measurable decline rates⁵. These statistics are summarised in Table 4.

In the next section, we estimate the distances and extinction of the sample, which requires the observed peak magnitudes of both bands. Of the 1371 SNe with an estimated s_{gr} , 1289 have observed peaks in both the g and r bands or a spectroscopic redshift. Out of the 82 that do not, one is very dim, with $s_{gr} < 0.4$, which accounts for 25 per cent of the SNe in this s_{gr} regime. The observed peak statistics of the BTS sample are summarised in Table 5.

A table with all the data used to construct the LF from the BTS SNe is given in Appendix D. The table includes the s_{gr} values, method used for their estimation (directly or the relevant decline rate parameter), decline rate parameters, estimated peak magnitudes, and M_{Ni56} (see Section 6).

Table 4. BTS color stretch parameter statistics.

Criteria	# of SNe	Comments
With s_{gr}	1371	
s_{gr} directly	204	
s_{gr} from Δm	1167	
s_{gr} from $\Delta m_{15}(r)$	8	only for $\Delta m_{15}(r) > 1$, with CSP fit
s_{gr} from $\Delta m_{15}(g)$	853	only for $\Delta m_{15}(g) < 1.55$
s_{gr} from $\Delta m_8(g)$	208	SNe with $\Delta m_8(g) > 0.54$ are fit with combined fit
s_{gr} from $\Delta m_{30}(r)$	98	
No s_{gr} , $\Delta m_{15}(r) < 1$	89	
No recognized peaks	30	
Less than 5 epochs in both bands	16	
Undetermined	13	
Total # of SNe	1519	

⁵ SN 2019fch had a peak g value from a single photometric measurement that was much higher than the peak r value and resulted in a very large $\Delta m_8(g)$. These values were inconsistent with its $E(g-r)_h$ evaluation or its typical $\Delta m_{15}(r)$ value, so we discarded this SN.

Table 5. BTS observed peak statistics.

Criteria	# of SNe
All SNe with s_{gr}	1371
with peak r	1319
with peak g	1299
with peak g and r	1247
with peak g and r or spec. distance	1289

4 COMPLETENESS AND VOLUME-LIMITED SAMPLE

In this section, we investigate the completeness of the BTS sample. For the LF to represent the true distribution, the sample in each luminosity bin should be either complete or volume-corrected. In order to analyse the sample's completeness, we consider a narrow range of peak luminosities, where the survey can be considered as volume-limited, with the observed volume determined by the chosen luminosity. We choose to use the r band, because of the higher number of SNe with a peak magnitude in this band, and because of the more uniform K -correction in this band, as compared to the g band. The cumulative comoving distance distribution of each luminosity bin should behave with distance like $\propto V \sim D^3$, assuming the SNe are uniformly distributed in the considered volume. This behaviour is expected to hold until $D = D_{\text{lim}}(s_{gr})$, the distance where the observed magnitude reaches the limiting magnitude of the survey. In reality, the behaviour is more complicated because of, e.g., extinction and incomplete classification. We analyse the completeness of the BTS survey using the spectroscopic redshifts, when available, and our method for determining the distances for the SNe that lack spectroscopic redshifts, as described below. We first use the CSP peak magnitude– s_{gr} relation (applying a K -correction, which is somewhat different from the K -correction of P20, see Appendix B for details). Then, we can write the differences between absolute and observed magnitudes in each band (for the 1247 SNe with both g and r observed peak magnitudes) as:

$$\begin{aligned} M_g &= m_g - \mu - A_g^{\text{gal}} - A_g^{\text{h}} \\ M_r &= m_r - \mu - A_r^{\text{gal}} - A_r^{\text{h}}, \end{aligned} \quad (5)$$

with the three unknown parameters: μ , the distance modulus, A_g^{h} , the host extinction in the g band, and A_r^{h} , the host extinction in the r band. In order to solve for the three unknowns, we assume a uniform ratio of the total-to-selective extinction $R_r = A_r^{\text{h}}/E(g-r)_{\text{h}} \approx 1.4$, where $E(g-r)_{\text{h}} = A_g^{\text{h}} - A_r^{\text{h}}$. This value, which corresponds to $R_V \approx 1.5$, minimizes the mean error between the estimated distances and the distances to the SNe with spectroscopic distances, to ~ 7 per cent. This value of R_r is also close to the mean value of $R_r \approx 1.6$ that was obtained in our analysis of the SNe with spectroscopic distances (see Section 9), and is typical for SNe Ia hosts (Burns et al. 2018). Using a higher value of $R_r = 2.8$, which corresponds to the Milky Way extinction law $R_V = 3.1$, increases the total rate by ~ 15 per cent, but does not have a significant effect on the shape of the LF. SNe with negative values of $E(g-r)_{\text{h}}$ were not corrected for host extinction.

Figure 7 shows the s_{gr} -distance distribution of the SNe in our sample, where the x -axis is scaled as D^3 . SNe with distances calculated using the methods described above are shown as black circles, and SNe with spectroscopic distances are shown as blue circles. Dashed curves show the maximal visible distance for several values of extinction and a $m = 18.5$ mag limiting magnitude. These values are chosen to represent three s_{gr} regimes (see Section 9 and Appendix C). The red line shows D_{break} (see below) for each s_{gr} bin.

The black vertical line at 180 Mpc marks the distance of our volume-limited LF, where most of the sample is approximately complete. As can be seen in the figure, the SNe are more concentrated at low distances, and their density becomes lower before the distance reaches the zero host-extinction limiting distance.

We next plot the comoving distance distributions for several s_{gr} bins in Figure 8, where the x -axis is scaled as D^3 . For each bin, a curve of $(D/D_{\text{lim}})^3$, assuming zero extinction, is also plotted in a black solid line. As can be seen in the figure, all distributions deviate from the D^3 law at some distance $D_{\text{break}} < D_{\text{lim}}$. This is due to Milky Way and host galaxy extinction that increase the magnitude of events that are within the observed volume to above the limiting magnitude, and possibly due to incomplete classification of dim events. In order to estimate D_{break} , we find the highest distance where the maximal deviation of a linear fit to the cumulative fraction as a function of the volume is larger than 0.03. These fits are shown by black, dashed lines, and the break distance, D_{break} , is displayed in each panel. Also shown is the extinction required to decrease the limiting distance to the break distance, given by:

$$A_r^{\text{break}} = 10^{\frac{D_{\text{lim}} - D_{\text{break}}}{5}}. \quad (6)$$

This quantity roughly marks the extinction that affects a non-negligible fraction of the SNe for each s_{gr} bin. As can be seen in Figure 8, SNe with large s_{gr} values suffer from large extinction values of $A_r^{\text{break}} \approx 1.5$ mag (the implication of this result is further discussed in Section 10), while the distribution of SNe with low and medium values of s_{gr} are affected only at lower values, $A_r \lesssim 1.1$ mag. This is in agreement with the host extinction distributions obtained in Section 9 and presented in Figure 13. However, the break distance for low-luminosity SNe, with $s_{gr} \lesssim 0.8$, is lower than expected from the typical extinction values of these SNe, and possibly related to incomplete classification.

In Appendix C, we study in detail different choices to limit the sample (either in volume or in magnitude) in order to reach a balance between statistic and systematic errors. We find an optimum with a 180 Mpc volume-limited sub-sample (indicated in Figure 7) with 298 SNe in the considered time range (see Appendix C for details regarding the LF time range), which require a non-negligible volume correction only for the dimmest bin. We verify in Appendix C that different choices to limit the sample provide consistent results, although with larger errors (statistical or systematic). In the next section, we construct the LF from the 180 Mpc volume-limited sub-sample.

5 LUMINOSITY FUNCTION CONSTRUCTED FROM THE COLOUR STRETCH PARAMETER

After obtaining the color stretch parameter s_{gr} for the vast majority of the BTS sample and choosing a sub-sample that is nearly complete, we can construct the LF by differentiating Equation (1) with respect to the chosen parameter (e.g., s_{gr} , M_r). The calculation and comparison of LFs from different sub-samples are described in Appendix C.

The s_{gr} distribution is shown in Figure 1. As can be seen in the figure, the distribution peaks at $s_{gr} \approx 1$ and drops monotonically on both sides, up to $s_{gr} \approx 1.3$ at the high end and down to $s_{gr} \approx 0.35$ at the low end. However, this is probably not the lower limit, as SN 2006mr from the CSP sample has a color stretch value of $s_{gr} \approx 0.3$. The upper limit marks the highest rate to detect no events at 95 per cent confidence for an s_{gr} bin size of 0.1. We show in Section 7

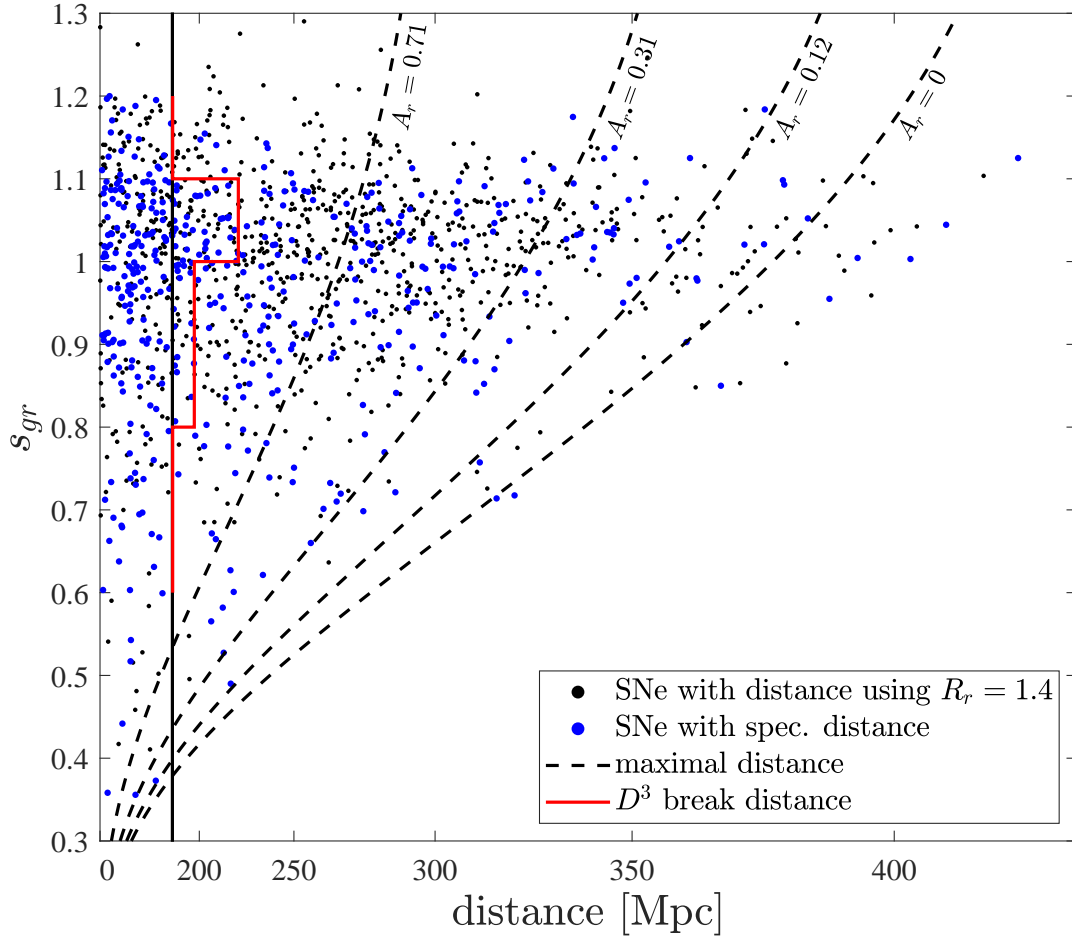


Figure 7. The s_{gr} -distance distribution of the SNe in the sample, where the x -axis is scaled as D^3 . Black circles denote the SNe with distances calculated with the methods described in the text, while SNe with spectroscopic distances are marked by blue circles. Dashed curves show the maximal visible distance for several extinction values and a $m = 18.5$ mag limiting magnitude. The extinction values represent the typical extinction of several s_{gr} bins (see Section 9 and Appendix C). The red line indicates, for each s_{gr} bin, the distance from where the D^3 law breaks, according to Figure 8. The black vertical line at 180 Mpc marks the distance of our volume-limited LF.

that the s_{gr} distribution is consistent with a unimodal, featureless distribution.

The LF of the peak r magnitude is shown in Figure 2. The volume-corrected (-uncorrected) rates are indicated by blue (red) symbols. Only the dimmest bin requires a non-negligible volume correction. The PLF of P20, where the BTS absolute magnitudes are calculated using the estimated redshift, is presented as green symbols. The LFs are scaled so that the total rate matches the total rate obtained in this work, which is calculated by integrating the LF. Also plotted is the PLF of the LOSS survey (Li et al. 2011a), scaled to match the total rate and shown with respect to the R filter used in the LOSS survey. The x -axis is shifted so that the LOSS peak's location matches the other LFs. The upper limit is the same as in Figure 1. Despite the similar observation lengths (although the observation dates are different, see Appendix C), the upper limits of the low-luminosity SNe in this work are higher than in P20 because we included a host extinction completeness factor (see Appendix C) that reduces the observed volume, and the bin size used in our analysis is smaller by ≈ 35 per cent, increasing the chance that a SN in an empty bin will be missed. The g -band peak magnitude LF is similar to the r band, and is not shown here.

As can be seen in Figure 2, the LF of this work peaks at $M_r \approx -19.2$, in agreement with P20. However, the rate of more luminous

and dimmer events drops much more rapidly than in P20, where the rate of peak magnitudes dimmer than $M_r \gtrsim -19$ mag is higher by almost an order of magnitude than in this work. In addition, the PLF of P20 reaches low-luminosity values of $M_r \approx -16.7$ mag, while our dimmest events have peak magnitudes of $M_r \approx -17.5$ mag. As explained in Section 2, this is the result of distance uncertainties and the host extinction being neglected in P20, which smears the PLF in comparison to our derived LF, where distance estimates are more accurate and host extinction is taken into account. We obtained a total SN Ia rate of $2.91^{+0.58}_{-0.45} \times 10^4 \text{ Gpc}^{-3} \text{ yr}^{-1}$, higher than the result of P20, $\approx 2.35 \times 10^4 \text{ Gpc}^{-3} \text{ yr}^{-1}$. The error indicates the statistical uncertainty due to $1 - \sigma$ Poisson noise. The total rate drops to $2.56^{+0.58}_{-0.46} \times 10^4 \text{ Gpc}^{-3} \text{ yr}^{-1}$ when the observation dates are the same as in P20, within ≈ 10 per cent of their total rate. This is a good consistency check of our procedure, as the total rates derived from the LF and the PLF should be similar (neglecting the host extinction in the PLF leads to larger volume corrections, which are compensated by the larger maximal observed volume in Equation (2), calculated assuming zero extinction).

Though the range of magnitudes is not as wide, the LOSS PLF is quite similar to P20 (but with larger error-bars, as the LOSS sample size is smaller), since the host extinction is neglected also

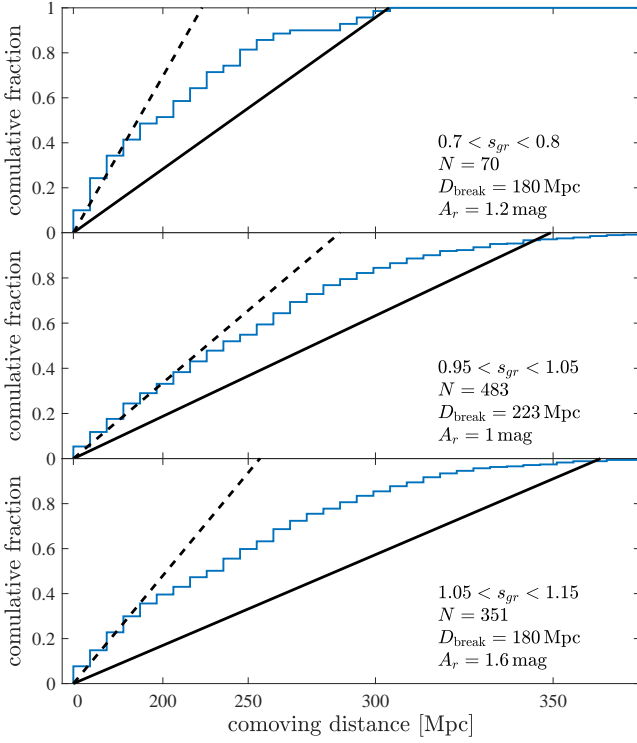


Figure 8. Cumulative fraction of SNe as a function of the comoving distance for different representative s_{gr} bins, where the x -axis is scaled as D^3 , so that the observed volume increases linearly. For each s_{gr} bin, we present the plot of the $(D/D_{lim})^3$ curve (black, solid line) and $(D/D_{break})^3$ (black, dashed line). The number of SNe in the bin, N , the break distance, D_{break} , and the corresponding extinction according to Equation (6), A_r^{break} , are indicated in each panel.

when calculating the LOSS PLF. We study the LOSS sample in more detail in Appendix A.

6 THE ^{56}Ni MASS DISTRIBUTION

In this section, we transform the distributions calculated in Section 5 to a $M_{\text{Ni}56}$ distribution, which is more useful for constraining models. This is done by using the CSP sample to calibrate a relation between s_{gr} and $M_{\text{Ni}56}$. We use the sample of 20 SNe from (Sharon & Kushnir 2020b) with derived $M_{\text{Ni}56}$, supplemented with an additional 5 SNe, where $M_{\text{Ni}56}$ is calculated using the methods of Sharon & Kushnir (2020b). The bolometric luminosity, photometry, and processed photometry for the additional SNe is given in the supplementary material.

The obtained relation between s_{gr} and $M_{\text{Ni}56}$ is shown in the middle panel of Figure 1. As can be seen in the figure, s_{gr} and $M_{\text{Ni}56}$ are tightly correlated (scatter of $\sim 0.03 M_{\odot}$), where the best fit of the form:

$$M_{\text{Ni}56}/M_{\odot} = p_0 + p_1 s_{gr} + p_2 s_{gr}^2, \quad (7)$$

is plotted with a solid line and its parameters are given in Table 6.

Using Equation (7), we evaluate $M_{\text{Ni}56}$ for each SN in the BTS sample with an estimated s_{gr} value. Then, using the same procedure as in the previous section, we calculate the $M_{\text{Ni}56}$ distribution of the BTS sample. The result is shown in blue symbols in the bottom panel of Figure 1. As can be seen in the figure, the rate peaks at $M_{\text{Ni}56} \approx 0.6 M_{\odot}$, and there are no other distinguishable peaks. The

Table 6. Properties of the $M_{\text{Ni}56}$ fits with respect to s_{gr} and s_{BV} for the CSP SNe (Equations (7) and (A1)).

parameter	fit variable	p_0	p_1	p_2	N^a	χ^2/dof	scatter
$M_{\text{Ni}56}/M_{\odot}$	s_{gr}	-0.11	0.37	0.34	16	0.31	0.03
$M_{\text{Ni}56}/M_{\odot}$	s_{BV}	-0.19	0.62	0.18	20	0.19	0.03

^a Number of objects used to determine the fit

rate of dim ($M_{\text{Ni}56} \lesssim 0.3 M_{\odot}$) and luminous ($M_{\text{Ni}56} \gtrsim 0.8 M_{\odot}$) events is significantly lower than the rate of typical $M_{\text{Ni}56}$ events. We show in Section 7 that the $M_{\text{Ni}56}$ distribution is consistent with a unimodal, featureless, distribution.

Piro et al. (2014) constructed the $M_{\text{Ni}56}$ distribution (red symbols in the figure), using the volume-limited LOSS survey (Leaman et al. 2011; Li et al. 2011a). $M_{\text{Ni}56}$ was estimated from the B band decline rate, $\Delta m_{15}(B)$, using the equation:

$$M_{\text{Ni}56}/M_{\odot} = 1.34 - 0.67 \Delta m_{15}(B). \quad (8)$$

We perform our own analysis on the LOSS survey, and obtain the $M_{\text{Ni}56}$ through the color stretch parameter s_{BV} (green symbols in the figure). A detailed description is provided in Appendix A. To allow comparison between the two LOSS distributions, in the figure, the total rates of both LOSS distributions were normalized to match the BTS total rate. All the distributions peak at roughly the same mass, $M_{\text{Ni}56} \approx 0.6 M_{\odot}$, and behave quite similarly at $0.4 M_{\odot} \lesssim M_{\text{Ni}56} \lesssim 0.7 M_{\odot}$. Differences arise at the low and high $M_{\text{Ni}56}$ regimes. In the low-luminosity end, the rate of the BTS LF is smaller and drops more or less monotonically with $M_{\text{Ni}56}$, while the behaviours of the LOSS distributions are more erratic. Additionally, the dip in the s_{BV} distribution of the LOSS sample (see Appendix A) remains after the transformation to $M_{\text{Ni}56}$ ($0.2 M_{\odot} \lesssim M_{\text{Ni}56} \lesssim 0.4 M_{\odot}$), and a secondary peak appears at $\approx 0.2 M_{\odot}$. This secondary peak also appears in the distribution of Piro et al. (2014), which is explained there as a large fraction of 91bg-like events. However, the secondary peak is not seen in the BTS results, and it is therefore most likely a result of the low number statistics of the LOSS survey (consistent with the large error bars of this bin). The small sample size might also explain the erratic behavior of the LOSS distribution throughout the entire dim end and the differences at the luminous ($M_{\text{Ni}56} \gtrsim 0.7$) end.

A note is in place regarding the sharp peak of the LF (Figure 2) compared with the more smooth distribution of the $M_{\text{Ni}56}$ (bottom panel of Figure 1). While the LF's sharp peak is somewhat driven by our procedure that uses the peak magnitude – s_{gr} relation, which ignores the small scatter around this relation (see Figure 4), the main reason for the difference between the distributions is the nonlinear relation between $M_{\text{Ni}56}$ and the peak magnitude. The vast majority of SNe have $M_{\text{Ni}56} \sim 0.3 - 0.8 M_{\odot}$ (see Figure 1), and since the peak flux is roughly proportional to $M_{\text{Ni}56}$, this range of $M_{\text{Ni}56}$ is ~ 1 mag in magnitude space. Additionally, the logarithmic definition of magnitude forces a narrower spacing of high $M_{\text{Ni}56}$ values compared to lower values, which makes the LF appear very narrow, as the $M_{\text{Ni}56}$ distribution is already concentrated at relatively high $M_{\text{Ni}56}$ values.

7 THE DERIVED DISTRIBUTIONS ARE CONSISTENT WITH UNIMODAL, FEATURELESS, DISTRIBUTIONS

The LF and the distributions of this work are based on the shape parameter s_{gr} . Given the non-negligible errors in the evaluation of this parameter, we examine the effects of these errors on the derived

distributions and check whether the small features seen in the results are consistent with a unimodal, featureless distribution. We do this by guessing an underlying distribution, and with MC simulations, we calculate the distribution that would be observed after applying random errors to the s_{gr} values. We can then compare the simulated distribution to the observed distribution in order to constrain the parameters of the underlying distribution and the errors that are applied to it. The underlying s_{gr} distribution is given by one rising and one decaying exponential:

$$R(s_{gr}) = \begin{cases} C \times (\exp(s_{gr}/\tau_1) - 1) & 0 \leq s_{gr} \leq \mu \\ R(s_{gr} = \mu) \cdot \exp(-(s_{gr} - \mu)/\tau_2) & s_{gr} \geq \mu \end{cases}, \quad (9)$$

where τ_1 and τ_2 are the scale parameters and μ is the turnover point. The rate of the rising exponential is modified so that it is zero for $s_{gr} = 0$, and the decaying exponential is multiplied by $R(s_{gr} = \mu)$ for continuity. Parameter C is the overall normalization. This model includes five free parameters: two scale parameters (τ_1, τ_2), one turnover points (μ), the overall scale and the s_{gr} (Gaussian) error.

A Markov Chain Monte Carlo (MCMC), using the `mcmcstat` MATLAB package⁶ is performed in order to find the distribution of the parameters and their best fit to the observed distribution. The results are shown in the upper panel of Figure 9. The red shaded area shows the 68-per-cent confidence levels of the underlying distribution, where the red line within marks the median. The best-fit model distribution lies within the shaded region and is similar to the median distribution, although it is somewhat narrower. The observed distribution is presented by green symbols, and the best-fit model distribution after applying error realizations by yellow symbols. The error for the best-fit model distribution is the 68-per-cent confidence bounds of the error realizations using the same underlying best-fit distribution parameters. As expected, the resulting underlying distribution is somewhat narrower than the observed one, since applying errors widens the distribution. The best-fit distribution is within the error margin of the observed distribution, and reproduces it quite well. The obtained error in s_{gr} is ~ 0.028 , which is lower than the BTS mean estimated s_{gr} uncertainty of ~ 0.11 . However, the s_{gr} uncertainties, given by SNooPy through MC simulations, might be overestimated, and the low χ^2 values of the BTS fits in Table 3 support this claim. The parameters of the underlying distributions are: $\mu = 1.14^{+0.02}_{-0.02}$, $\tau_1 = 0.22^{+0.03}_{-0.02}$, $\tau_2 = 0.017^{+0.013}_{-0.014}$, and $C = 8.5^{+5.0}_{-3.2} \times 10^2 \text{ Gpc}^{-3} \text{ yr}^{-1}$.

In the lower panel of Figure 9 we show the same results for the M_{Ni56} distribution. We use the same underlying distribution with the parameters that were found for the s_{gr} distribution, transformed using Equation (7). The best-fit results also agree with the observed M_{Ni56} distribution.

The total rate of the underlying LF is $R \approx 2.81^{+0.72}_{-0.62} \times 10^4 \text{ Gpc}^{-3} \text{ yr}^{-1}$, consistent with the total rate of the observed LF. We conservatively add to the Poisson noise the error due to the uncertainty of the fitted model parameters. We obtain for the iron production rate $1.61^{+0.36}_{-0.32} \times 10^4 M_{\odot} \text{ Gpc}^{-3} \text{ yr}^{-1}$.

The results in this section show that the features on top of the unimodal-derived distributions are all consistent with statistical noise on top of featureless distributions. The derived distributions, therefore, suggest a single progenitor channel for the explosions.

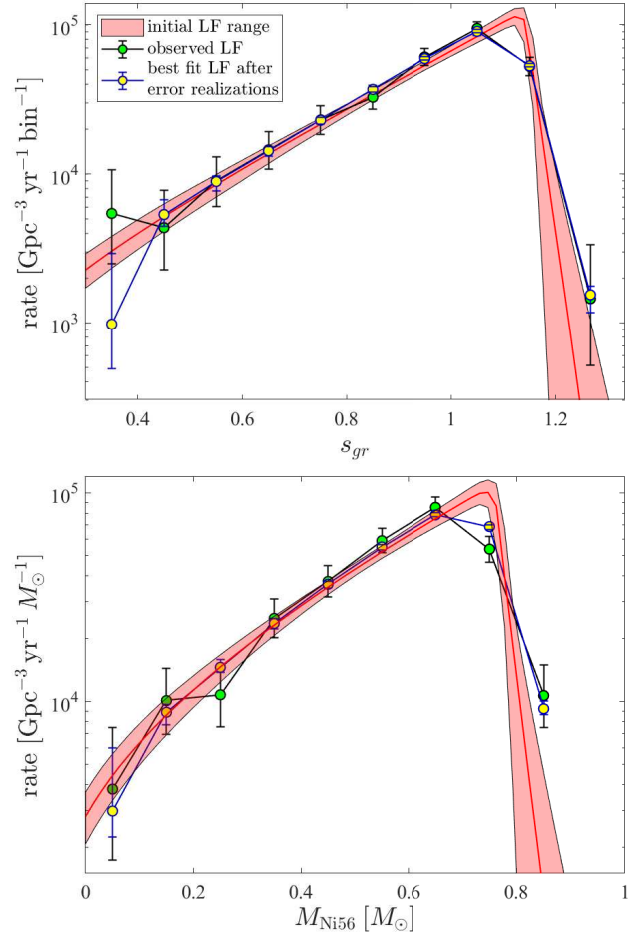


Figure 9. Upper panel: Model s_{gr} distribution and best-fit after error realizations. Shown are the 68-per-cent confidence levels of the underlying distribution (red shaded area) and its median (red line), together with the observed distribution (green symbols) and the best-fit distribution after error realizations (yellow symbols). Lower panel: same as the upper panel for the M_{Ni56} distribution. The parameters of the underlying and best-fit distributions are the same as those of the s_{gr} distribution; the distribution was transformed using Equation (7).

8 GALAXY TYPE COMPARISON

In this section, we calculate the M_{Ni56} distribution in different types of galaxies for the 180 Mpc sub-sample. We follow the procedure in P20, where galaxy types are determined according to the absolute i magnitude and the $g - i$ color of the host galaxy. The hosts were required to be in the SDSS photometric field, and have redshift values between $0.015 < z < 0.1$. P20 found that the color of the SNe Ia hosts forms a bimodal distribution, with a "red sequence", dominated by early type galaxies, and a "blue cloud" that consists mostly of spirals and irregulars, separated by a "green valley". The distinction between the different types of galaxies is given in table 2 of P20.

We use the same host types as in P20 (note that the 180 Mpc sub-sample is well within the redshift upper limit), and we recalculate the LF and the M_{Ni56} distribution for each type. We apply an additional global correction of ≈ 1.71 that takes into account the fraction of SNe that are in the SDSS photometric field. The results are shown in Figure 10. Note that the SDSS field requirement introduces a selection bias (possibly distance-dependent), which in-

⁶ <https://mjlaine.github.io/mcmcstat/>

roduces systematic biases to our results in this section (for example, the black lines in the figure do not exactly match the distributions in Figure 1). As can be seen in the figure, the relative rates strongly depend on the galaxy type. The red-sequence galaxies are the main hosts of low-luminosity events, with ≈ 82 per cent of the SNe with $M_{\text{Ni56}} \lesssim 0.4$ found to explode in these galaxies. Additionally, the fraction of low-luminosity SNe is ≈ 23 per cent of the whole sample, and ≈ 36 per cent of the red sequence. Luminous events of $M_{\text{Ni56}} \gtrsim 0.7$ take place mostly in the blue cloud spiral and irregular galaxies, which host ≈ 53 per cent of these SNe. For the green valley distributions, the fraction of dim (luminous) events is lower (higher) than the red sequence and higher (lower) than the blue cloud. The results are in qualitative agreement with the results of Ashall et al. (2016) and the results of LOSS in Li et al. (2011a). It is also consistent with our analysis of the LOSS sample, although we do not provide the LOSS LF for different types of galaxies, as it contains a small number of SNe in each galaxy type.

9 HOST EXTINCTION ANALYSIS

In this section, we estimate the distribution of the host galaxy extinction for SNe Ia, using the BTS and the LOSS samples. The LOSS sample includes accurate distances to the SNe, but lacks host galaxy extinction evaluation, as it is not required for the calculation of the PLF. In Appendix A, we present a reanalysis of the LOSS sample, in which we calculate absolute magnitudes from the light-curve shape parameters. We can therefore use the known distances and galactic extinction A_x^{gal} , the observed magnitudes and the estimated absolute magnitudes to estimate the host extinction A_x^{h} in some band x :

$$A_x^{\text{h}} = m_x - M_x - \mu - A_x^{\text{gal}}. \quad (10)$$

The results are shown in the top panels of Figure 11, where the distributions of the estimated host extinction in the V and B bands are shown for two groupings of host galaxy types: spiral and irregular galaxies (red-filled bars) and elliptical and lenticular galaxies (empty black bars). Note that the galaxy types are grouped differently than in Li et al. (2011a). Around 10 per cent of A_V^{h} and ~ 6 per cent of A_B^{h} have negative extinction values, which is the result of the error in the observed peak value and of the intrinsic scatter of the absolute magnitude fit.

We can further calculate the selective extinction, $E(B - V)_h = A_B^{\text{h}} - A_V^{\text{h}}$, and the ratio of the total-to-selective extinction, $R_V^{\text{h}} = A_V^{\text{h}} / E(B - V)_h$. The results are shown in the bottom panels of Figure 11. For the R_V^{h} results, we only consider SNe with $E(B - V)_h > 0.1$ and positive A_V^{h} and A_B^{h} . Smaller values of $E(B - V)_h$ result in large, unrealistic values of R_V^{h} for several SNe, since the extinction at these values is comparable to its uncertainty. However, there are still a few SNe with $R_V^{\text{h}} > 4$, which is probably due to these errors.

The figures show that most SNe exhibit some amount of host extinction, and a non-negligible fraction are highly reddened by their host. All the SNe with large extinction values are known to be highly reddened, such as 2003cg (Elias-Rosa et al. 2006), 1999cl (Krisciunas et al. 2017) and 2006X (Wang et al. 2008). As expected, extinction is stronger in spiral and irregular galaxies, and its distribution in these galaxies shows a tail extending up to ≈ 3 mag in the V band. SNe in early type galaxies also suffer from reddening values of a few tenths of a magnitude, but no more than 1 mag. The distribution of R_V^{h} is mostly between 1 – 4, (with a few

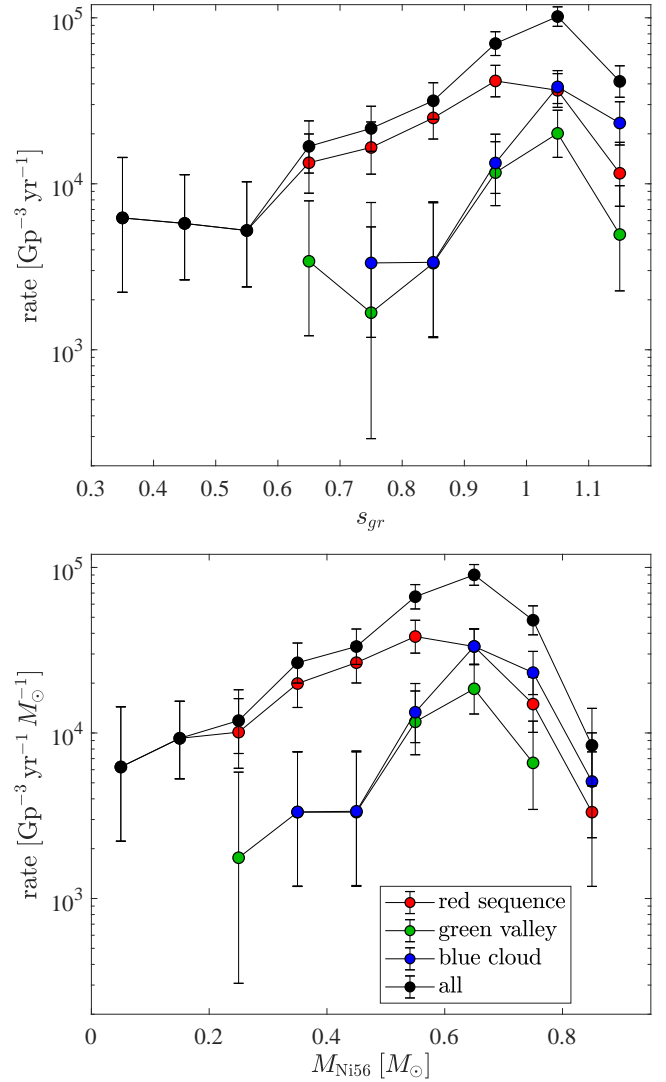


Figure 10. BTS volume-corrected distributions for different galaxy types. Top panel: s_{gr} . Red sequence, green valley, and blue cloud galaxies are shown as red, green, and blue symbols, respectively. See table 2 of P20 for details about the classification procedure. The total distribution is shown as black symbols. Only SNe in the SDSS photometric field are considered, so the distribution of all the galaxies does not exactly match the distribution in Figure 1. Bottom panel: same as the top panel for M_{Ni56} . The red sequence, which contains early-type galaxies, is much more skewed towards dim events, while normal and luminous events occur mostly in the blue cloud, which contains spirals and irregulars.

outliers that have higher values), but the sample size is rather low and biased towards SNe with large extinction values.

Determining the distribution of the BTS host galaxy extinction is more difficult, as most SNe have no accurate distances, and the ones that do might have some selection bias. Nonetheless, we have calculated the host extinction in the g and r bands for 455 SNe with spectroscopic redshifts and measured s_{gr} with the same method as above, including K -corrections. Because of the low number of objects in this analysis, we did not apply a volume limit as in the previous sections; rather, we include all the objects that passed our criteria (with a proper volume correction, see below). The selective extinction, $E(g - r)_h = A_g^{\text{h}} - A_r^{\text{h}}$, can be calculated from the observed magnitudes and the absolute magnitudes for all SNe (if they have

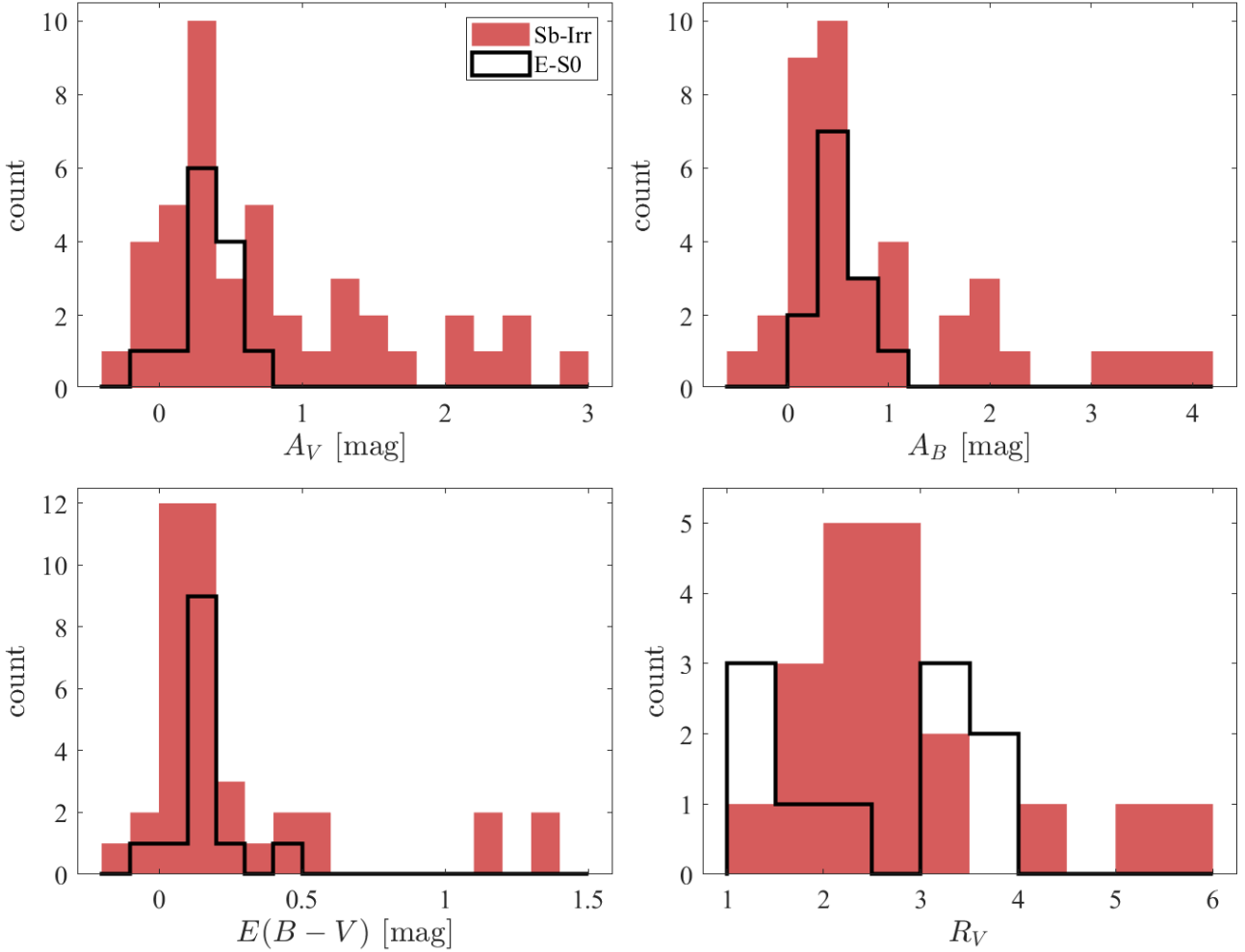


Figure 11. Distributions of the estimated host extinction in the V and B bands, the selective host extinction $E(B - V)_h$, and the ratio of the total-to-selective extinction R_V^h of the LOSS sample. Sb-Irr galaxies are shown in red-filled bars, and E-S0 galaxies in black, empty bars.

an observed peak magnitude measurement in both bands), since it is independent of distance:

$$E(g - r)_h = m_g - M_g - (m_r - M_r) - (A_g^{\text{gal}} - A_r^{\text{gal}}) \quad (11)$$

Figures 12 and 13 show the distributions of the host galaxy extinction A_r^h (upper left panel), A_g^h (upper right panel), the selective extinction of all SNe, $E(g - r)_h$ (lower left panel), and the ratio of the total-to-selective extinction, $R_r^h = A_r^h / E(g - r)_h$. The relations to the Johnson B and V bands are given by $E(g - r) / E(B - V) \approx 0.8 - 1$ and $R_V / R_r \approx 1.13 - 1.17$ for R_V values in the range 1–4. In Figure 12, the distributions are divided into galaxy types, classified as in Section 8, while in Figure 13, the distributions are divided into s_{gr} bins. The distributions are volume-corrected according to their luminosities and their host extinction value, modifying Equation (2) to

$$V_{\text{max},i} = \frac{4\pi}{3} \left(10^{\frac{m_{\text{lim}} - M_i - A_{x,i}^h}{5} - 8} \right)^3 \text{ Gpc}^3. \quad (12)$$

This correction substantially increases the weights of high-extinction SNe, and may bias the distribution when the sample size is small. This is the case for the A_r^h and A_g^h distributions of the

$s_{gr} > 1.15$ bin, where the sample size is 13 SNe and the extinction values are relatively high. Therefore, these distributions have been supplemented with error bars that illustrated the high uncertainty. The uncertainties of the other distributions are much smaller, and are not shown for visualization purposes. The R_r distribution only contains SNe with $E(g - r)_h > 0.2$ mag and $A_g^h, A_r^h > 0.1$.

The BTS A_r^h and A_g^h distributions resemble the LOSS host extinction distribution, with an extinction value of a few 0.1 mag for most SNe and a tail of high extinction values. The typical uncertainties in the calculation of the extinction are larger for BTS than for LOSS because of larger errors in the observed peak magnitudes and color stretch values. The mean error in the observed r peak magnitude is ≈ 0.05 mag, and the mean error in the absolute peak magnitude due to the uncertainty in the color stretch is ≈ 0.13 mag, so their root sum squared is ≈ 0.14 mag. Variations in the K -corrections and the filter transmission function might also contribute to the error. Therefore, the fraction of SNe with a negative extinction is higher, reaching ≈ 13 per cent and ≈ 10 per cent in the r and g bands, respectively, and is ≈ 17 per cent for $E(g - r)_h$.

In order to quantify the host extinction distribution and the

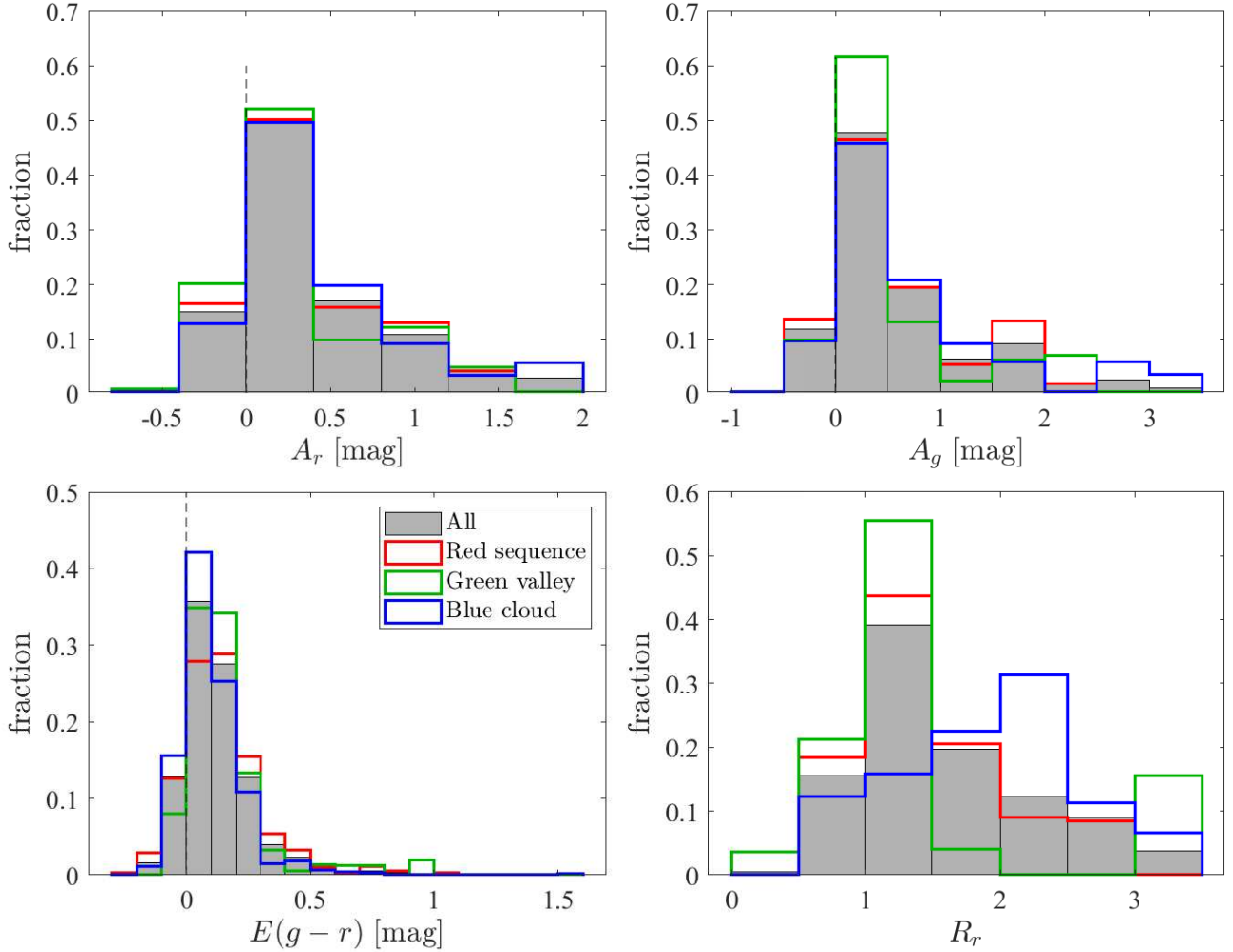


Figure 12. Distributions of the host galaxy extinction of the BTS sample. Upper-left (right) panel: A_r^h (A_g^h) distribution of the BTS SNe with spectroscopic redshifts for different galaxy types. All the distributions are volume-corrected and normalized by the total count of the whole sample. Lower left panel: The selective host extinction $E(g-r)_h$ distribution for the whole sample. Lower right panel: The ratio of the total-to-selective extinction R_r^h for SNe with $E(g-r)_h > 0.2$ mag.

observational errors, we fitted a three-parameter model of a gamma distribution that represents the intrinsic extinction distribution, convolved with a Gaussian that represents the extinction uncertainty:

$$f(A_r^h) = \Gamma(k, \theta) * \mathcal{N}(0, \sigma^2), \quad (13)$$

where $\Gamma(k, \theta)$ is the gamma distribution with a shape parameter k and a scale parameter θ , and $\mathcal{N}(0, \sigma^2)$ is a Gaussian with a zero mean and a standard deviation σ . The results of k and θ are highly affected by the binning method, but the results of the Gaussian standard deviation and the distribution mean are much more stable. The Gaussian standard deviation is $\sigma \approx 0.11$ – 0.14 , and is consistent with the uncertainties in the observed and absolute peak magnitudes. The fitted distribution mean is $E[A_r^h] \approx 0.49$ – 0.54 mag, and is consistent with the mean of the observed distribution of ≈ 0.46 mag. Fitting the same model for $E(g-r)_h$ results in a standard deviation of $\sigma \approx 0.065$ and a mean at $E[E(g-r)_h] \approx 0.11$ mag, while the mean of the observed distribution is also 0.11 mag.

The A_r^h and A_g^h distributions show that highly reddened SNe are more common in the blue cloud than in the red sequence. However,

we do not find considerable differences between the galaxy types in the $E(g-r)_h$ plot. This might be the result of the large errors in the extinction, or the insufficiency of the galaxy type classification, which is based on the host color and absolute magnitude for this analysis. From the R_r^h distribution, it can be gleaned that blue-cloud galaxies favour large R_r^h values, in comparison to the red sequence. The differences in Figure 13 are more pronounced, and there are no low s_{gr} SNe with an A_r^h or A_g^h larger than 1 mag. However, this may be the result of an observational bias, since these SNe are intrinsically dim and would be hard to detect if they are highly reddened as well.

The large s_{gr} SNe are characterized by exceptionally high extinction values. These results are consistent with the relatively small distances at which these SNe are complete (see Section 4), which is smaller than the distances of dimmer SNe. The small sample size of large s_{gr} SNe does not allow us to accurately measure the shape of the A_r^h and A_g^h distributions at high extinctions. This situation could be improved with future observations (see discussion in Section 10).

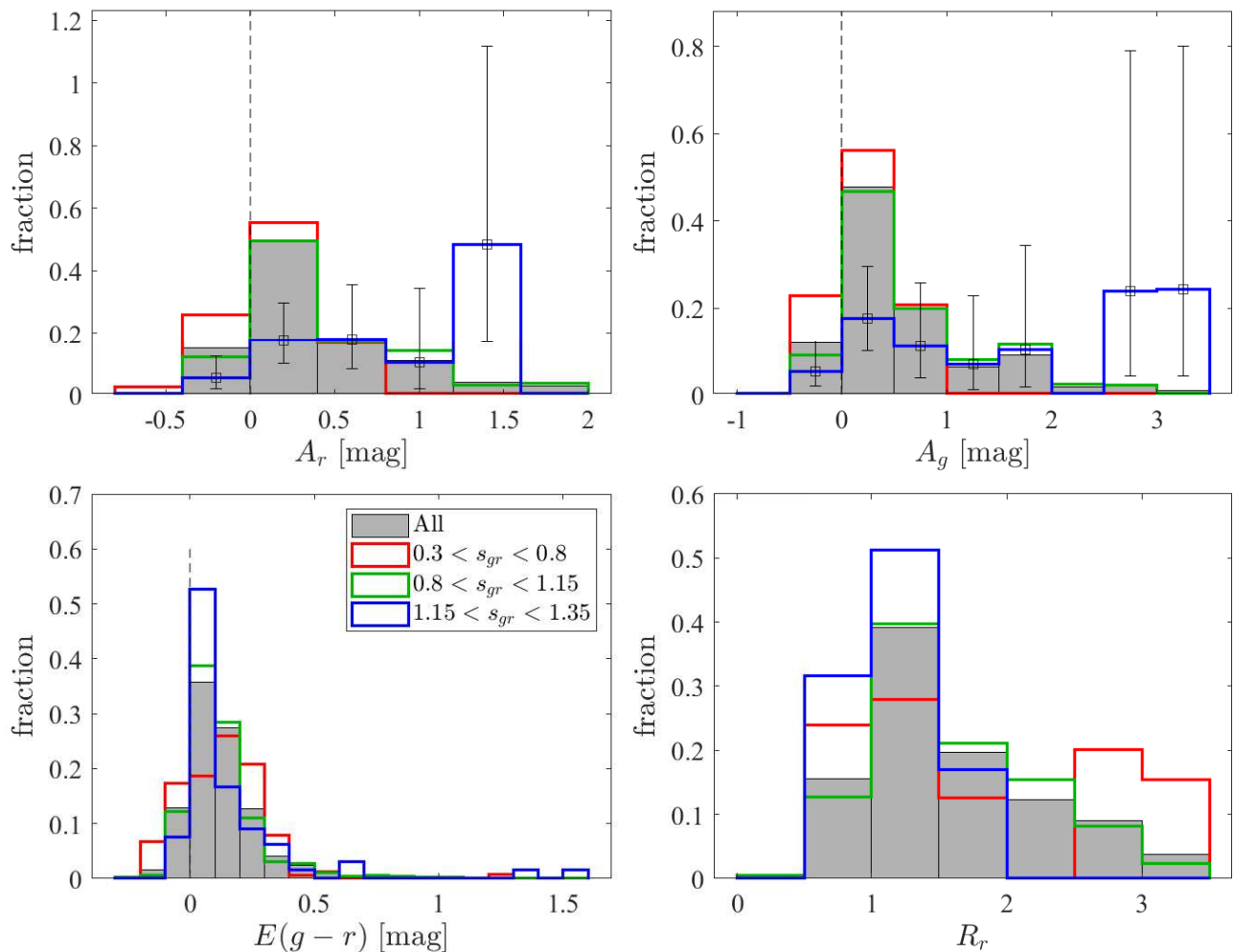


Figure 13. Distributions of the host galaxy extinction of the BTS sample for different s_{gr} ranges. Upper left (right) panel: The A_r^h (A_g^h) distribution of the BTS SNe with spectroscopic redshifts for different s_{gr} bins. All the distributions are volume-corrected, and error bars are shown for the $s_{gr} > 1.15$ bin distribution. Lower left panel: The selective host extinction $E(g-r)_h$ distribution for the whole sample. Lower right panel: The ratio of the total-to-selective extinction R_r^h for SNe with $E(g-r)_h > 0.2$ mag and with positive extinction values in both bands.

10 SUMMARY AND DISCUSSION

In this work, we used the large ZTF BTS data set to construct the LF of SNe Ia. In general, constructing a LF requires knowledge of the redshift and host extinction for each SN, which is a difficult task to perform in a survey with a very high discovery rate such as the BTS. This challenge can be partly bypassed for SNe Ia, by using the tight correlations between the light curve color stretch, s_{gr} , and the intrinsic luminosity, calibrated from the CSP Ia sample (see Section 2, Figure 4). We determined the s_{gr} values of the vast majority of the SNe Ia in the BTS survey (Section 3) and we chose a 180 Mpc volume-limited sub-sample that is nearly complete (with 298 SNe, Section 4). We then constructed, for the first time, the intrinsic SNe Ia LF (Section 5, Figure 2). In Section 6, we used the CSP data to calibrate a novel tight relation between the s_{gr} and M_{Ni56} (middle panel of Figure 1), which served to construct the M_{Ni56} distribution of SNe Ia (bottom panel of Figure 1). We also constructed the SN Ia distribution for different galaxy types (Section 8, Figure 10), and, for the first time, the host galaxy extinction distributions (Section 9).

We find that the M_{Ni56} distribution peak at $\approx 0.6 M_\odot$, and

that the LF peaks are at an r magnitude of $M_r \approx -19.2$, in agreement with previous results. The rate of dim and luminous events, with $M_{Ni56} \lesssim 0.4 M_\odot$ or $M_{Ni56} \gtrsim 0.8 M_\odot$, is lower by at least a factor of 5 than the rate at the peak. We find a total rate of $R \approx 2.91^{+0.58}_{-0.45} \times 10^4 \text{ Gpc}^{-3} \text{ yr}^{-1}$ (per comoving element in the redshift range $z \approx [0.01, 0.04]$), consistent with previous studies (Dilday et al. 2010; Graur et al. 2011; Li et al. 2011b; Frohmaier et al. 2019; Perley et al. 2020). This result has an additional non-negligible systematic error due to uncertainties in the correction factors (e.g., host extinction and the K -correction), and is probably a few tens of a percent. A detailed estimate of the survey’s efficiency (see, e.g., Frohmaier et al. 2019) is required in order to establish the systematic uncertainty of the total rate.

The dimmest end of the LF in this work is at $M_r \approx -17.5$ mag. While dimmer SNe Ia exist, such as SN 2007mr (Burns et al. 2018), the non-detection of such events within our sample is an indication of their rarity. The ZTF Census of the Local Universe (CLU; De et al. 2020) reported additional low-luminosity SNe Ia, SN 2019gau and SN 2019ofm. These objects have peak magnitudes of -16.75 mag and -16.84 mag, respectively. However, the quality

of their light-curves does not allow one to determine their intrinsic luminosity from the light-curve shape and it is unclear whether they are intrinsically dim or suffer from a large host extinction.

We performed MC simulations to show that the features on top of the unimodal-derived distributions are all consistent with statistical noise (Section 7). The derived distributions, therefore, suggest a single progenitor channel for the explosions.

We show that the red sequence galaxies are the main hosts of low-luminosity events, with ≈ 82 per cent of the SNe with $M_{\text{Ni}56} \gtrsim 0.4$ found to explode in these galaxies. Luminous events of $M_{\text{Ni}56} \gtrsim 0.7$ take place mostly in the blue-cloud spiral and irregular galaxies, which host ≈ 53 per cent of these SNe. These results are in a qualitative agreement with the results of Ashall et al. (2016) and the results of LOSS (Li et al. 2011a). From the host galaxy extinction distributions, we find mean values of $A_r^h \sim 0.5$ mag and $E(g-r) \sim 0.11$ mag, and that a non-negligible fraction of SNe, especially in star-forming galaxies, exhibit large extinction values, $\gtrsim 1$ mag, in the optical bands. We further find that a host galaxy's extinction highly depends on the luminosity of the SNe. A non-negligible fraction of the luminous SNe with $s_{gr} \gtrsim 1.15$ suffer from $A_r^h \gtrsim 1$ mag, with no low s_{gr} SNe exhibiting an A_r^h or A_g^h larger than 1 mag. These results are in line with the idea that luminous SNe Ia originate from young populations, while low-luminosity SNe Ia require old progenitors.

We conclude the discussion of SNe Ia LF with a visual summary of the considered surveys. Figure 14 shows the distance and absolute magnitude detection limits, for several extinction values, of the ZTF BTS (blue), LOSS (red), and CNla0.02 (black) surveys. The absolute r magnitudes, as calculated in this work, and the distances of the BTS SNe Ia calculated in this work (with spectroscopic redshifts), are marked by black (blue) circles. The LOSS sample distances and absolute peak V magnitudes, as calculated in this work, are shown as red circles. Despite the difficulties that arise in a large survey, the high cadence and the large distances at which the BTS classifies transients are unmatched by the other surveys. However, as we have shown, accurate distances are essential in order to calculate the LF. Acquiring the accurate redshift for all BTS hosts is possible, and would significantly improve the scientific output of the survey. For example, there are 100 SNe with $E(g-r)_h > 0.2$ and spectroscopic redshifts in our sample that comprise the R_r distribution (except for 8 with negative $A_g^h < 0.1$ or $A_r^h < 0.1$); obtaining the redshifts of all the SNe would increase this number to 241. This information is available for the CNla0.02 survey, which would allow the cross-checking of the results presented in this paper.

An accurate distance estimation is even more important for core-collapse SNe. As the photometric evolution of these SNe is more diverse than that of SNe Ia, it is more difficult to estimate their intrinsic luminosity from the light curve shapes, as we have done for SNe Ia. In addition, due to the younger environments of these SNe, the host extinction is probably higher, on average, than the ones we found for SNe Ia, leading to even higher uncertainties in their intrinsic luminosity. The transformation from the published PLF of these SNe (Li et al. 2011a, P20) to the intrinsic LF is, therefore, highly uncertain.

DATA AVAILABILITY

The data underlying this article are available in the article and in its online supplementary material.

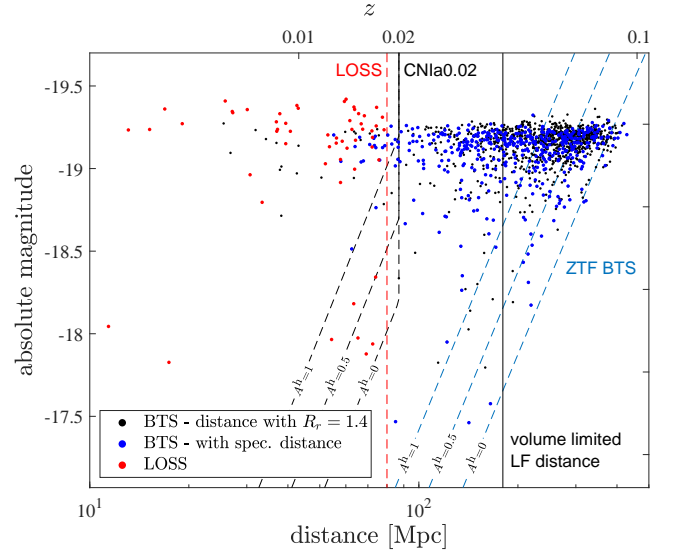


Figure 14. The distance-magnitude observation limits and SNe Ia distributions of several SNe surveys. The BTS observation limit is shown as blue, dashed lines for several host extinction values. The BTS SNe Ia with distances calculated in this work are shown as black symbols, and the SNe with spectroscopic redshifts as blue symbols. The peak magnitudes of these SNe are the ones determined in this work. The LOSS distance limit and SNe, with the peak V band magnitudes calculated in this work, are presented as a red dashed line and red symbols, respectively. The CNla0.02 observation limits for several extinction values are shown as black, dashed lines. The black solid line at 180 Mpc marks the distance of our volume-limited LF.

ACKNOWLEDGEMENTS

We thank Boaz Katz and Eran Ofek for useful discussions. DK is supported by the Israel Atomic Energy Commission –The Council for Higher Education –Pazi Foundation – by a research grant from The Abramson Family Center for Young Scientists and by ISF grant.

REFERENCES

- Ashall C., Mazzali P., Sasdelli M., Prentice S. J., 2016, *MNRAS*, **460**, 3529
- Ashall C., et al., 2020, *ApJ*, **895**, L3
- Bellm E. C., et al., 2019, *PASP*, **131**, 018002
- Burns C. R., et al., 2011, *AJ*, **141**, 19
- Burns C. R., et al., 2014, *ApJ*, **789**, 32
- Burns C. R., et al., 2018, *ApJ*, **869**, 56
- Chen P., et al., 2020, arXiv e-prints, p. arXiv:2011.02461
- Contreras C., et al., 2010, *AJ*, **139**, 519
- De K., et al., 2020, *ApJ*, **905**, 58
- Dilday B., et al., 2010, *ApJ*, **713**, 1026
- Elias-Rosa N., et al., 2006, *MNRAS*, **369**, 1880
- Fremming C., et al., 2020, *ApJ*, **895**, 32
- Frohman C., et al., 2019, *MNRAS*, **486**, 2308
- Graur O., et al., 2011, *MNRAS*, **417**, 916
- Graur O., Bianco F. B., Huang S., Modjaz M., Shivvers I., Filippenko A. V., Li W., Eldridge J. J., 2017a, *ApJ*, **837**, 120
- Graur O., Bianco F. B., Modjaz M., Shivvers I., Filippenko A. V., Li W., Smith N., 2017b, *ApJ*, **837**, 121
- Hakobyan A. A., Barkhudaryan L. V., Karapetyan A. G., Gevorgyan M. H., Mamon G. A., Kunth D., Adibekyan V., Turatto M., 2020, *MNRAS*, **499**, 1424
- Hicken M., et al., 2009, *ApJ*, **700**, 331
- Kochanek C. S., et al., 2017, *PASP*, **129**, 104502
- Kriszianus K., et al., 2017, *AJ*, **154**, 211
- Leaman J., Li W., Chornock R., Filippenko A. V., 2011, *MNRAS*, **412**, 1419

- Li W., et al., 2011a, *MNRAS*, **412**, 1441
- Li W., Chornock R., Leaman J., Filippenko A. V., Poznanski D., Wang X., Ganeshalingam M., Mannucci F., 2011b, *MNRAS*, **412**, 1473
- Maoz D., Mannucci F., Li W., Filippenko A. V., Della Valle M., Panagia N., 2011, *MNRAS*, **412**, 1508
- Maoz D., Mannucci F., Nelemans G., 2014, *ARA&A*, **52**, 107
- Ofek E. O., 2014, MAAT: MATLAB Astronomy and Astrophysics Toolbox (ascl:1407.005)
- Pakmor R., Kromer M., Taubenberger S., Springel V., 2013, *ApJ*, **770**, L8
- Perley D. A., et al., 2020, *ApJ*, **904**, 35
- Phillips M. M., 1993, *ApJ*, **413**, L105
- Phillips M. M., et al., 2013, *ApJ*, **779**, 38
- Piro A. L., Thompson T. A., Kochanek C. S., 2014, *MNRAS*, **438**, 3456
- Polin A., Nugent P., Kasen D., 2019, *ApJ*, **873**, 84
- Rodrigo C., Solano E., 2020, in Contributions to the XIV.0 Scientific Meeting (virtual) of the Spanish Astronomical Society. p. 182
- Ruiter A. J., et al., 2013, *MNRAS*, **429**, 1425
- Scalzo R. A., et al., 2019, *MNRAS*, **483**, 628
- Sharon A., Kushnir D., 2020a, *Research Notes of the American Astronomical Society*, **4**, 158
- Sharon A., Kushnir D., 2020b, *MNRAS*, **496**, 4517
- Shen K. J., Toonen S., Graur O., 2017, *ApJ*, **851**, L50
- Shivvers I., et al., 2017, *PASP*, **129**, 054201
- Soumagnac M. T., Ofek E. O., 2018, catsHTM: Catalog cross-matching tool (ascl:1810.013)
- Stritzinger M. D., et al., 2011, *AJ*, **142**, 156
- Taubenberger S., 2017, The Extremes of Thermonuclear Supernovae. p. 317, doi:10.1007/978-3-319-21846-5_37
- Wang X., et al., 2008, *ApJ*, **675**, 626
- Wygodna N., Elbaz Y., Katz B., 2019, *MNRAS*, **484**, 3941
- Yaron O., Gal-Yam A., 2012, *PASP*, **124**, 668

APPENDIX A: A REANALYSIS OF THE LOSS SAMPLE

The SNe of the LOSS sample (Leaman et al. 2011; Li et al. 2011a,b; Maoz et al. 2011) were mostly observed in the Johnson filters, specifically, with the B and V bands, and we assume that there are no significant differences between the LOSS and the CSP filters. We, therefore, use the color stretch parameter s_{BV} to estimate peak magnitude, which allows one to distinguish between the low luminosity events properly (Burns et al. 2018). We calculate the color stretch parameter and decline rates using SNooPy (Burns et al. 2011). When comparing our results of $\Delta m_{15}(B)$ to Piro et al. (2014), we find a small average deviation of 5 per cent. We obtain the light curves of 66 out of the 76 SNe in Li et al. (2011a)⁷. We are able to directly estimate the s_{BV} values of 37 SNe, while for another 20 SNe, we estimate s_{BV} using the decline rate parameters $\Delta m_8(B)$, $\Delta m_{15}(B)$, and $\Delta m_{15}(V)$. The s_{BV} values and the decline rates are given in Table D4, and the $s_{BV} - \Delta m$ distributions are shown in Figure A1.

While the LOSS SNe span the entire $\Delta m_{15}(B)$ range, the region $0.55 \lesssim s_{BV} \lesssim 0.75$ contains only one SN. This is in contrast to the ZTF BTS sample, where the SNe span the entire s_{gr} range. We attribute this to the low number of SNe in the LOSS sample, an issue further discussed in Section 6.

We use observations in the B and V bands of the CSP sample to relate the color stretch s_{BV} to M_{Ni56} and to the peak magnitudes. We use a second-order polynomial for M_{Ni56} :

$$M_{Ni56}/M_{\odot} = p_0 + p_1 s_{BV} + p_2 s_{BV}^2, \quad (\text{A1})$$

and similar expressions for the peak magnitudes with $\ln(s_{BV})$ as the argument. The coefficients of the peak magnitudes fits and of the M_{Ni56} fit are given in Tables 2 and 6, respectively. Figure A2 shows the peak M_B (upper panel), peak M_V (middle panel), and M_{Ni56} (lower panel) values of the CSP sample as a function of s_{BV} . For each parameter, the fit to s_{BV} (or to $\ln(s_{BV})$) and the fit coefficients are displayed. The $M_{Ni56}-s_{BV}$ and $M_{Ni56}-s_{gr}$ distribution are very similar (Figure 1), as expected from the close relation between s_{gr} and s_{BV} (Ashall et al. 2020).

The LOSS SNe Ia survey has only minor completeness corrections, and we ignore them in this work. The obtained LF are shown and discussed in Section 6.

APPENDIX B: K-CORRECTIONS

In this section, we investigate the effects of the supernova redshift and of the filter transmission function on the observed decline rates and peak magnitudes. Since our analysis compares multiple surveys, the decline rates distribution could be affected by the specific parameters of each survey. This is apparent in Figure 6, where the $\Delta m_{15}(g)$ and $\Delta m_8(g)$ of the BTS sample have higher values than the CSP sample for the same s_{gr} . This could be potentially related to the filter transmission functions, where the Las Campanas Observatory filters (Stritzinger et al. 2011) are used by the CSP, and the Palomar observatory filters (Bellm et al. 2019) are used by the ZTF, and to the redshift distribution of the samples, as the BTS survey extends to higher redshifts. The mean redshift of the BTS sample is $z \approx 0.06$ ($z \approx 0.04$, and for the sub-sample with a direct s_{gr} measurement), while the mean redshift of the CSP sample is $z \approx 0.025$. We show below that the decline rate differences are mostly the result of the different characteristic redshifts of the two surveys.

Using the spectra of several well observed SNe Ia (see list in Figure B1), we measured the synthetic photometry of the g and r bands at multiple epochs for each SN. The spectra were taken from WiSeREP⁸ (Yaron & Gal-Yam 2012) and the filters transmission functions were taken from the SVO Filter Profile Service⁹ (Rodrigo & Solano 2020). Since the transmission functions of the ZTF filters does not include atmospheric extinction, we use the atmospheric transmission measured at the Kitt Peak National Observatory with an airmass of 1.1. For each epoch and SN, we measured the difference between the magnitude obtained with the CSP filter at the CSP typical redshift of $z = 0.025$, to the magnitude obtained with the ZTF filter at the BTS typical redshift of $z = 0.04$. The results are shown in Figure B1, where the values, shown in diamonds and solid lines, are shifted so that they are zero at peak time. Also plotted is the mean difference of all the SNe (black solid lines). As can be seen in the figure, the differences between the g magnitudes increase until ~ 20 day since peak. The dashed vertical lines mark 8 and 15 days after peak, and the dashed horizontal lines mark their intersection with the mean difference. The intersection values are ≈ 0.03 mag and ≈ 0.08 mag at 8 and 15 days after peak, respectively. This means that the g band decline rate values would increase for the filter and mean redshift of the BTS, compared to the CSP sample. The differences in the r band are less pronounced. To check whether the effect arises from the different filters or from the redshift difference, we also measured the differences using only the

⁷ The other 10 LOSS SNe have only clear band data (B. Stahl, private communication).

⁸ <https://wiserep.weizmann.ac.il>

⁹ <http://svo2.cab.inta-csic.es/theory/fps/>

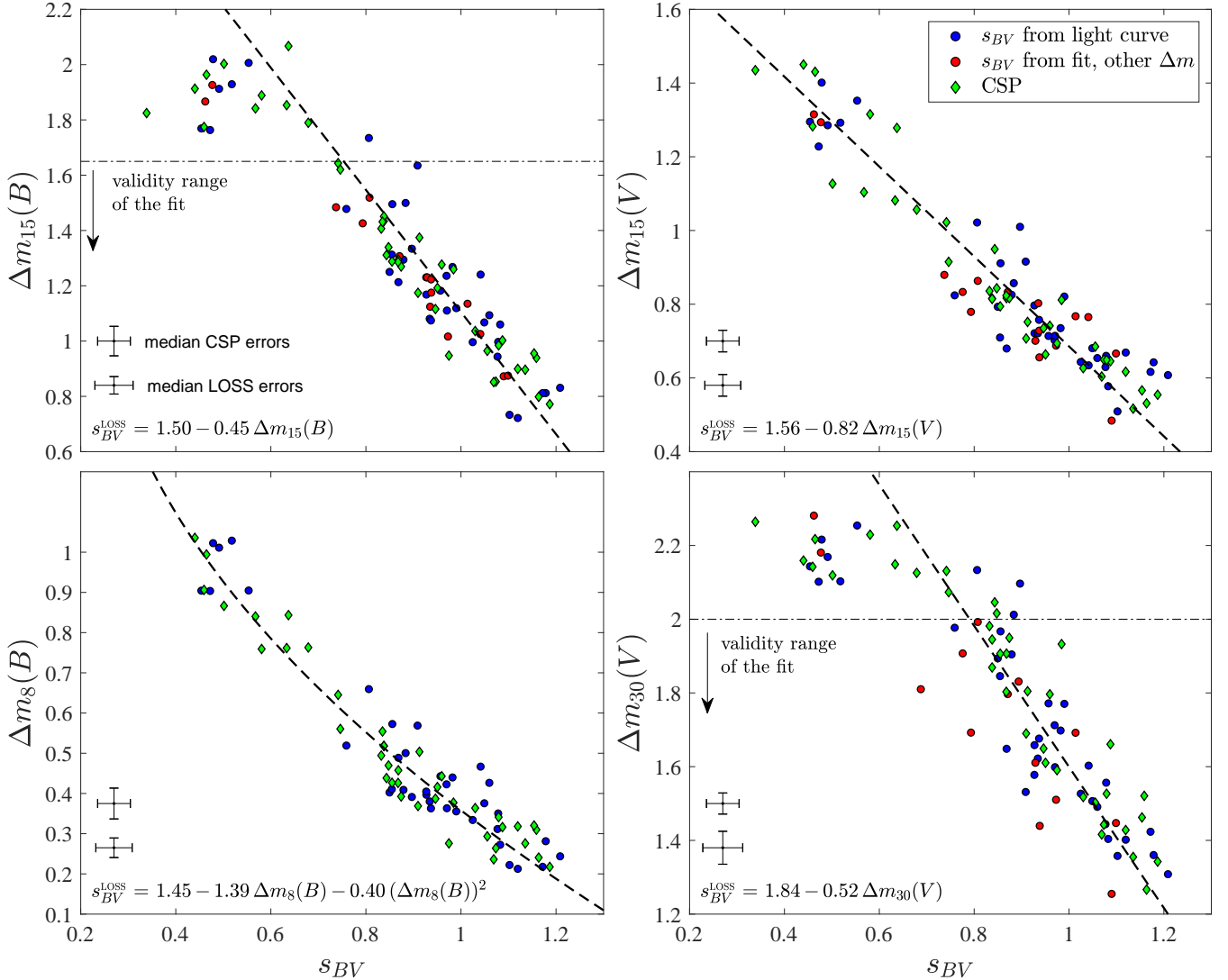


Figure A1. LOSS decline rate parameters as a function of s_{BV} . LOSS SNe with a direct s_{BV} measurement are shown as blue circles, while red circles correspond to SNe whose s_{BV} was determined using a different decline rate parameter. CSP SNe are shown as green diamonds. The median errors of the two samples is shown for each panel. The fits of the decline rate to the s_{BV} of the BTS and CSP samples are shown as a black, solid line and black dashed line, respectively. Also shown are the validity ranges of the $\Delta m_{15}(B)$ and $\Delta m_{30}(V)$ fits.

CSP filter for both redshift values. The results are shown in squares and dashed lines, and the mean difference in black dashed lines. This decreases the differences by ~ 30 per cent in the g band, so we conclude that they are mainly caused by the redshift differences. In the r band, the differences continue to be relatively small.

The difference between the g band decline rates obtained using the spectra agrees with the observed decline rate difference using photometry, where the fit of $\Delta m_{15}(g)$ to the s_{gr} is higher by ≈ 0.08 mag for the BTS sample, and the fit to $\Delta m_{30}(r)$ is almost identical (Figure 6). We confirmed that the color stretch values are unaffected in this exercise. This might also explain the scatter of the BTS decline rates seen in Figure 6, since the redshift of the BTS sample is distributed up to $z \sim 0.1$, although the typical uncertainties in the decline rate measurements dominate the scatter.

We have also studied the relations between the redshift and the peak magnitude of the ZTF and CSP filters. For this purpose, we measured the change of the peak magnitude as a function of the redshift that is applied to the spectra. For each SN, the spectra closest

to the peak time was chosen, and redshifted by several values, up to $z \sim 0.1$. We repeated this procedure for known low-luminosity SNe Ia. The results using the BTS filters are shown in Figure B2. As can be seen in the figure, the peak magnitude of normal SNe Ia becomes more luminous with the redshift in both the g and r bands, and its evolution is rather uniform among the different SNe. Low-luminosity SNe Ia have quite a different behaviour, especially in the g band. Also plotted is the K -correction used by P20 (dashed-dotted black line), which is linear to a good approximation for the observed range of redshift values, and a fit that consists of the mean difference of the normal SNe Ia of the BTS filters (solid black line) and the CSP filters (dashed black line). The mean r band correction of the fit is higher by a factor of ≈ 2.7 on average, and we use this fit for volume corrections throughout our analysis, and, together with the g band K -correction, for calculating the host extinction (see Section 9). The values of the fits for the BTS and CSP filters for several redshifts are given in Table B1. The dim SNe in Figure B2 have very low ^{56}Ni mass ($\sim 0.1 M_{\odot}$) and are a small part of

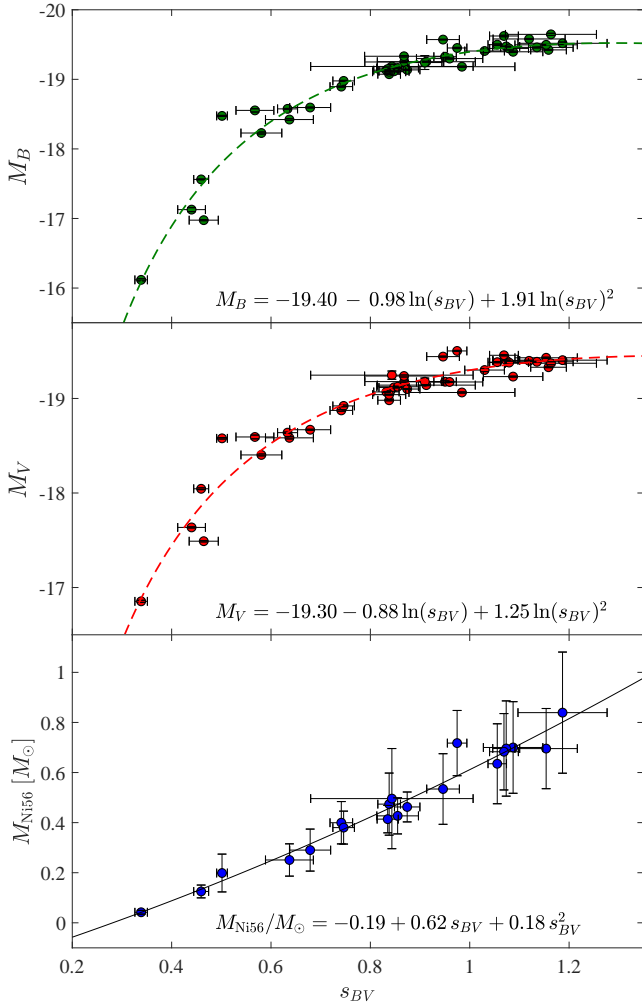


Figure A2. Peak M_B (upper panel), peak M_V (middle panel), and M_{Ni56} (lower panel) as a function of s_{BV} for the CSP sample. The fits are shown in lines, with the fit coefficients displayed at the bottom of each panel. The error bars for the peak magnitudes are smaller than the symbol size.

the sample, therefore we ignore them in our fit and apply a single correction function for all SNe based on normal SNe Ia.

Lastly, we used the SNe Ia spectra to calculate the peak magnitude difference between the CSP and the ZTF filters. Since we calibrate the absolute peak magnitude with the CSP sample and filters, this correction is required when calculating the distances, the volume corrections and the host extinction, where the observed magnitude is measured in the ZTF filters. To determine this correction, we once again chose the spectra closest to the peak time for each SN, and measured the difference between the synthetic magnitudes as a function of redshift. We performed the same procedure for normal and for low-luminosity SNe Ia (although we only use the correction for the normal SNe Ia). The results are presented in Figure B3. As can be seen in the figures, the difference behaviour is quite uniform for all non-low-luminosity SNe, with a scatter of $\lesssim 0.02$ mag. A curve showing the mean difference is shown in a black solid line, and its values for several redshifts are given in Table B2. The peak magnitudes are corrected using the mean difference of normal SNe Ia for each filter:

$$M^{ZTF} = M^{CSP}(s_{gr}) - \Delta M(z) \quad (B1)$$

where $M^{CSP}(s_{gr})$ is the peak magnitude given by the CSP fit and

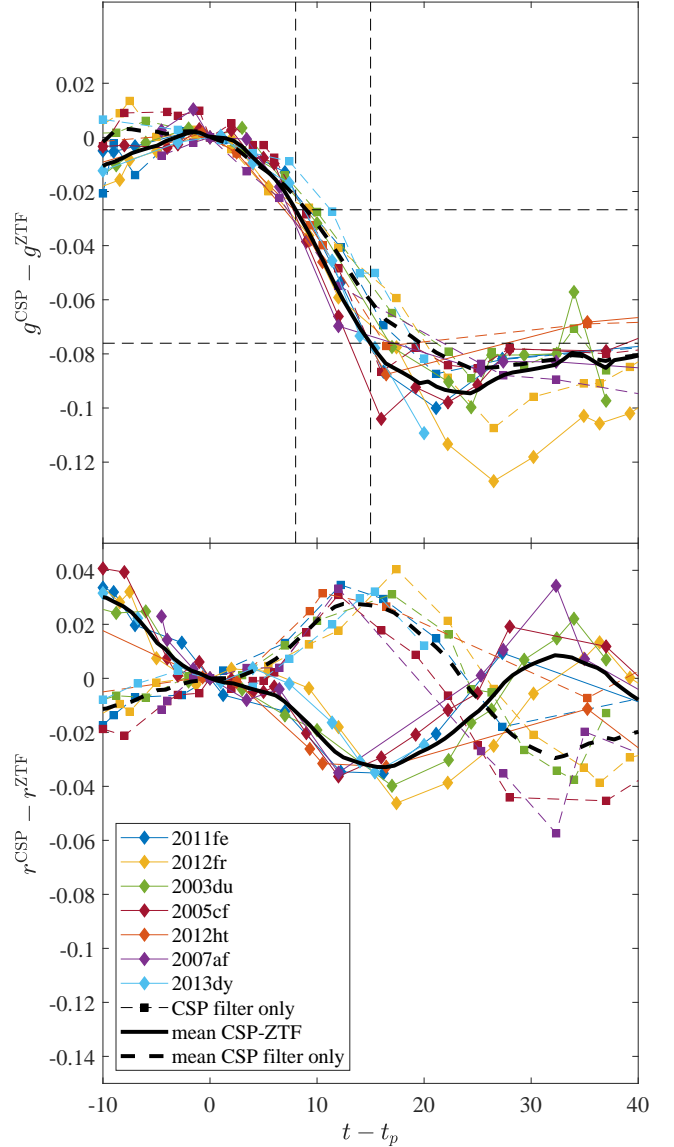


Figure B1. CSP and BTS synthetic magnitude difference as a function of the time since peak (top panel: g -band; bottom panel: r -band). The values for each SN are shifted so that they are zero at peak time. The differences between the CSP filter at the CSP typical redshift of $z = 0.025$ to the ZTF filter at the BTS typical redshift of $z = 0.04$ are shown in diamonds and solid lines. Squares and dashed lines show the results for the CSP filters where the only difference is the redshift. Black curves show the mean difference in both cases. The dashed vertical lines in the top panel mark 8 and 15 days after peak, and the dashed horizontal lines mark their intersection with the mean difference. The intersection values indicate the mean difference in the decline rate that would have been calculated.

$\Delta M(z)$ is the filter correction function. The correction function is given by a linear interpolation of the mean difference function using the redshift, as provided by the BTS explorer. Although we argue throughout this work that these redshift values are not accurate, the peak magnitude error resulting from this uncertainty is small. This correction has a small effect on the LF, but a substantial effect on the selective extinction $E(g-r)_h$, reducing the fraction of SNe with negative $E(g-r)_h$ from ≈ 41 per cent to ≈ 17 per cent.

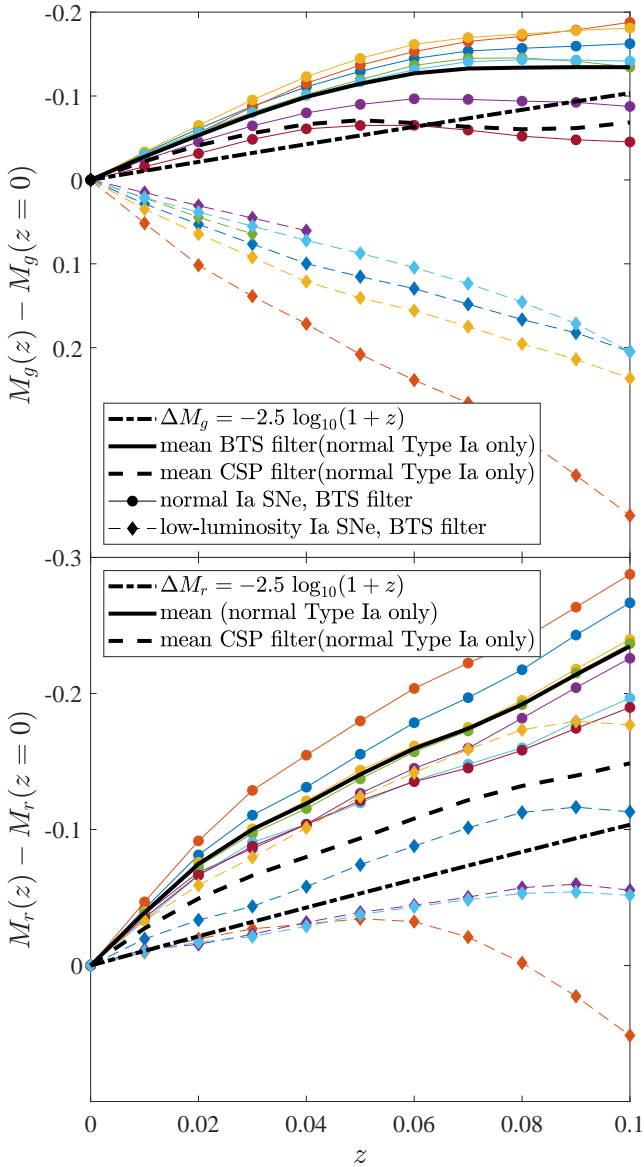


Figure B2. Top panel: The change in the synthetic g band peak magnitude as a function of redshift, calculated with the BTS filter transmission function for several SNe Ia. The solid (dashed) black line indicates the mean BTS (CSP) curve, while the dashed-dotted black line indicates the correction given by P20. Bottom panel: Same as the top panel for the r band. The normal SNe Ia are: 2011fe, 2012fr, 2003du, 2005cf, 2012ht, 2007af, 2013dy. The low-luminosity SNe are: 2005ke, 2005bl, 1999by, 1998de, 2006mr, 2007ax.

APPENDIX C: CONSTRUCTION OF THE LF AND VOLUME CORRECTIONS

In this section, we describe a few different methods for calculating the LF and we compare between volume-limited LF and magnitude-limited LF. Specifically, we show that a 180 Mpc volume-limited sub-sample is an optimal choice for balancing between statistical and systematic errors. We verify that different limits on the sample provide consistent results, although with larger errors (statistical or systematic).

For the calculation of the LF, we only consider SNe from March 15, 2019, as the detection and classification rate of the BTS had substantially increased compared to earlier epochs (see Figure 13 in P20), narrowing the sample size to 1371 SNe. In all the

Table B1. The g and r peak magnitude K -correction of the BTS and CSP filters. The function values are the mean peak magnitude difference of the considered SNe.

z	BTS ΔM_g	BTS ΔM_r	CSP ΔM_g	CSP ΔM_r
0.00	0.000	0.000	0.000	0.000
0.01	-0.028	-0.039	-0.022	-0.027
0.02	-0.053	-0.075	-0.041	-0.049
0.03	-0.078	-0.100	-0.055	-0.066
0.04	-0.099	-0.119	-0.065	-0.080
0.05	-0.115	-0.140	-0.069	-0.094
0.06	-0.127	-0.160	-0.065	-0.108
0.07	-0.133	-0.174	-0.060	-0.122
0.08	-0.134	-0.192	-0.057	-0.132
0.09	-0.134	-0.214	-0.058	-0.140
0.10	-0.134	-0.235	-0.064	-0.149

Table B2. The g - and r -peak magnitude correction function used in Equation (B1). The function values are the mean peak magnitude difference of the considered SNe.

z	ΔM_g	ΔM_r
0.00	-0.021	-0.081
0.01	-0.016	-0.069
0.02	-0.009	-0.055
0.03	0.001	-0.047
0.04	0.012	-0.042
0.05	0.024	-0.034
0.06	0.041	-0.029
0.07	0.051	-0.028
0.08	0.056	-0.021
0.09	0.055	-0.007
0.10	0.049	0.005

rest of the analysis, the whole sample of 1519 SNe is used. There is also a gap in March 2020 caused by bad weather that we take into account, so the total observation time of the LF is 2.27 years. the classification efficiency $f_{cl,i}$ remains the same as in P20. We measure the recovery fraction of the BTS sample at the considered times to be ≈ 0.68 , slightly higher than the value in P20, measured at different observation dates. Since we only use SNe with an estimated s_{gr} and observed peak g and r magnitudes (note that one observed peak is sufficient for the magnitude-limited LF), we apply additional global corrections, i.e., we divide by the fraction of SNe with an estimate for s_{gr} and by the fraction of SNe with estimated distances (≈ 0.9 for each factor; see Section 4 for details regarding the distance estimation).

The calculation of the magnitude-limited LF is similar to the procedure described in P20, but the volume corrections in Equation (2) are based on the estimated peak magnitudes of the r band. Additionally, the LF has another global correction factor that takes into account the reduction of the effective volume due to host extinction (note that this factor is not required for the construction of the PLF). For a given extinction A_r^h , the fractional volume reduction is:

$$\frac{V_{A_r^h}}{V_0} = 10^{-\frac{3}{5}A_r^h}, \quad (C1)$$

where $V_{A_r^h}$ is the observed volume for an extinction value A_r^h and some limiting magnitude. To calculate the mean fractional volume reduction, we use the host extinction distribution from Section 9, f_{A_r} :

$$f_{ext,h} = \left\langle \frac{V_{A_r^h}}{V_0} \right\rangle = \int dA_r^h f_{A_r} 10^{-\frac{3}{5}A_r^h} \approx 0.65, \quad (C2)$$

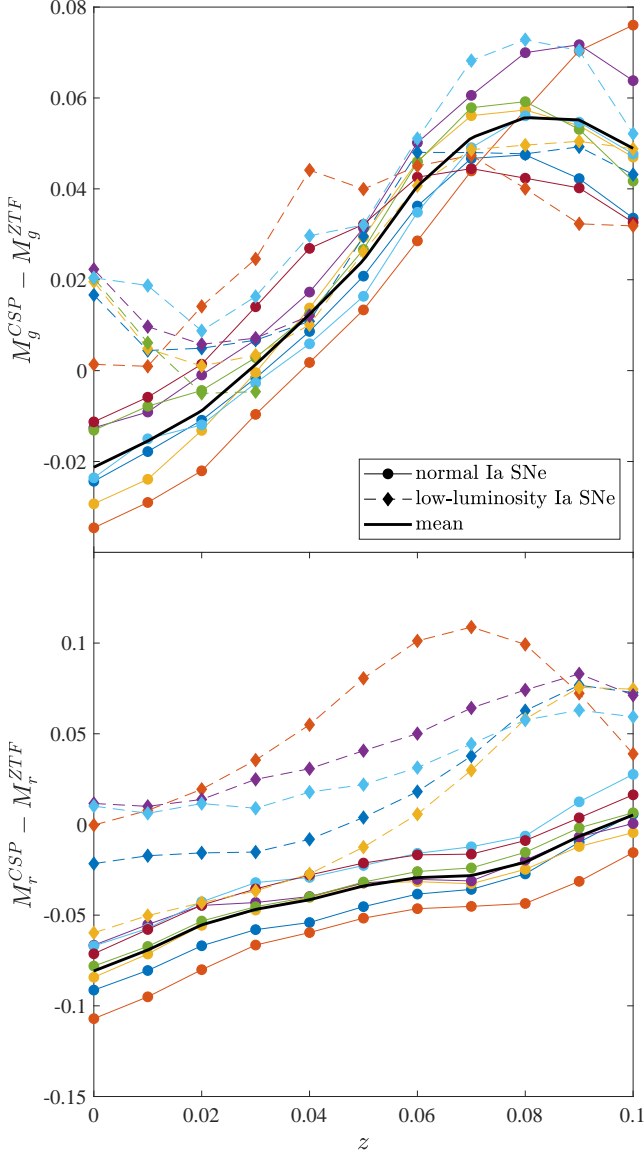


Figure B3. Top panel: Difference between the synthetic g band peak magnitude calculated with the CSP filter and with the ZTF filter, as a function of redshift. The solid black line indicates the mean curve. Bottom panel: Same as the top panel for the r band. The normal SNe Ia are: 2011fe, 2012fr, 2003du, 2005cf, 2012ht, 2007af, 2013dy. The low-luminosity SNe are: 2005ke, 2005bl, 1999by, 1998de, 2006mr, 2007ax.

which increases the SN Ia rate by ≈ 50 per cent.

The volume-limited LF is constructed from the SNe in the chosen volume, $V_{\text{LF}} = 4\pi D_{\text{LF}}^3/3$, with the weights in Equation (1) differing only because of the small variation in the classification efficiency, $w_i = (f_{\text{cl},i} V_{\text{LF}})^{-1}$. In contrast to the magnitude-limited LF, a global correction factor for the Milky Way and host extinction is not applied (the other factors remain). However, as can be seen in Figures 8 and 7, volume corrections are still required for dim-enough SNe, depending on the chosen distance, D_{LF} . The simplest form of correction is to correct for SNe with $D_{\text{lim}} < D_{\text{LF}}$, where D_{lim} is the limiting distance, neglecting galactic and host extinction:

$$D_{\text{lim}} = 10^{\frac{m_{\text{lim}} - M_i}{5}} - 5 \text{ Mpc}^3. \quad (\text{C3})$$

This correction increases the weights to $w_i = (f_{\text{cl},i} V_{\text{lim}})^{-1}$, where

V_{lim} is the volume corresponding to D_{lim} . As can be seen in Section 4, the sample is not uniformly distributed in D^3 up to D_{lim} , so this correction is an underestimate. Since the host extinction distribution depends strongly on s_{gr} (see Figure 13), each s_{gr} value has a different correction. In order to take into account the host extinction when applying the volume correction, we use again the host extinction distributions of Section 9. In this case, we divide the distribution into the three regimes of Figure 13: $s_{gr} < 0.8$, $0.8 < s_{gr} < 1.15$ and $s_{gr} > 1.15$. For each distribution f_{A_r} , we calculate the mean volume reduction using Equation (C2). We find that the corresponding extinction values for each bin are:

$$\langle A_r^h \rangle = -\frac{5}{3} \log \left(\left\langle \frac{V_{A_r^h}}{V_0} \right\rangle \right) = \begin{cases} 0.16 \text{ mag} & s_{gr} < 0.8 \\ 0.34 \text{ mag} & 0.8 < s_{gr} < 1.15 \\ 0.71 \text{ mag} & s_{gr} > 1.15. \end{cases} \quad (\text{C4})$$

Note that $\langle A_r^h \rangle$ is not the mean extinction and is always smaller than it. A similar value for the Milky Way extinction can be calculated from the volume reduction in P20, $f_{\text{ext,MW}}$:

$$\langle A_r^{\text{MW}} \rangle = -\frac{5}{3} \log (f_{\text{ext,MW}}) = 0.144 \text{ mag}. \quad (\text{C5})$$

Together, the maximal distance of each SN is modified by:

$$D_{\text{lim}} \rightarrow D_{\text{lim}} \times 10^{-\frac{\langle A_r^h \rangle + \langle A_r^{\text{MW}} \rangle}{5}}. \quad (\text{C6})$$

The curves of the modified distance for the three values of Equation (C4) are shown in Figure 7 in black, dashed lines. The volume corrections are then applied as above, by using the modified distance.

A different method that can be utilized to correct for the extinction is to use the entire host distribution in each s_{gr} bin and to sum the corrections for the extinction values that reduce the limiting distance below D_{LF} . When using this method, the weight of each SN is:

$$w_i = \frac{1}{f_{\text{cl},i}} \times \left(\int dA_r f_{A_r} \min \left\{ V_{\text{LF}}, V_{\text{lim}} \times 10^{-\frac{3}{5} (\langle A_r^h \rangle + \langle A_r^{\text{MW}} \rangle)} \right\} \right)^{-1}. \quad (\text{C7})$$

The corrections provided by this method are equal or larger than the corrections obtained with the previous method. However, these modifications have a small effect on the LF for the chosen distance of 180 Mpc.

The s_{gr} distributions are shown in Figure C1. The figure shows the volume-corrected (uncorrected) distribution in solid (dashed) lines, where the volume correction was applied using Equation (C6). As expected from Figure 8, the rates of the uncorrected LFs are considerably lower for $D_{\text{LF}} \gtrsim 250$ Mpc, since the survey is not complete at these distances for all luminosity bins. At $D_{\text{LF}} = 400$ Mpc, the total rate is less than half the rate at 180 Mpc.

The volume-corrected distributions are in better agreement with each other, and their total rate typically deviates by ~ 5 to ~ 10 per cent from each other. The figure also shows the magnitude-limited distribution of the SNe with both g and r observed peaks (black symbols), and the magnitude-limited distribution of all SNe (cyan symbols). The differences between the two magnitude-limited distributions are minor, except for the dimmest bin, $s_{gr} < 0.4$, that has a ≈ 25 per cent difference due to one SN with no observed peaks in both the g and r bands. The magnitude-limited distributions are in agreement with the volume-corrected distributions, with rates higher in low-luminosity bins and lower in high-luminosity bins. This is because the host extinction correction factor of the magnitude-limited distributions affects all bins equally, while the

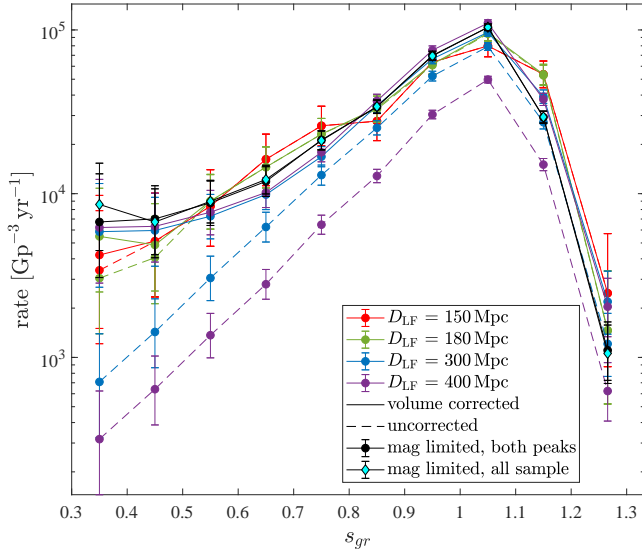


Figure C1. Comparison between the volume-limited s_{gr} distributions at various distances and the magnitude-limited distributions. Volume-corrected (uncorrected) distributions are shown as solid (dashed) lines, and the magnitude-limited distribution of SNe with both g and r observed peaks (all SNe) is shown as black (cyan) symbols. The volumetric rates for the uncorrected distributions at $D_{LF} \gtrsim 250$ Mpc are significantly lower in all bins, as the sample is not complete at these distances for all luminosity bins. At $D_{LF} \lesssim 200$ Mpc, the differences are mainly in the very dim and very luminous bins. The corrected distributions are in better agreement with each other. The magnitude-limited distributions are mostly in agreement with the volume-corrected distributions, with differences arising in high luminosity bins, where the impact of the host extinction is the largest.

impact of host extinction, as seen in Sections 4 and 9, is much more prominent in high-luminosity bins. The magnitude-limited total rate is within ~ 5 per cent of the volume-limited rates, and within ~ 1 per cent of the rate of the 180 Mpc sub-sample that is used for the main results. We chose this distance because it is the largest distance where the vast majority of the luminosity bins are complete, and therefore, requires minimal volume corrections (which are inherently uncertain, and therefore, increase the systematic error).

APPENDIX D: CSP, BTS, AND LOSS SAMPLE PROPERTIES

Figure D1 shows the CSP decline rate parameters as a function of s_{gr} for the CSP SNe. We also provide in Tables D1 and D2 the CSP sample data used to calibrate the relations between the light curve shape parameter and the intrinsic luminosity of the SNe. The tables contain the color stretch parameter and the source used for its determination (directly or from which decline rate), decline rates, peak magnitudes and M_{Ni56} . The peak magnitudes and M_{Ni56} were calculated using the independent distance and extinction estimates, from the constructed bolometric luminosity.

We similarly provide in Tables D3 and D4 the data for the BTS and LOSS samples, respectively.

This paper has been typeset from a T_EX/L^AT_EX file prepared by the author.

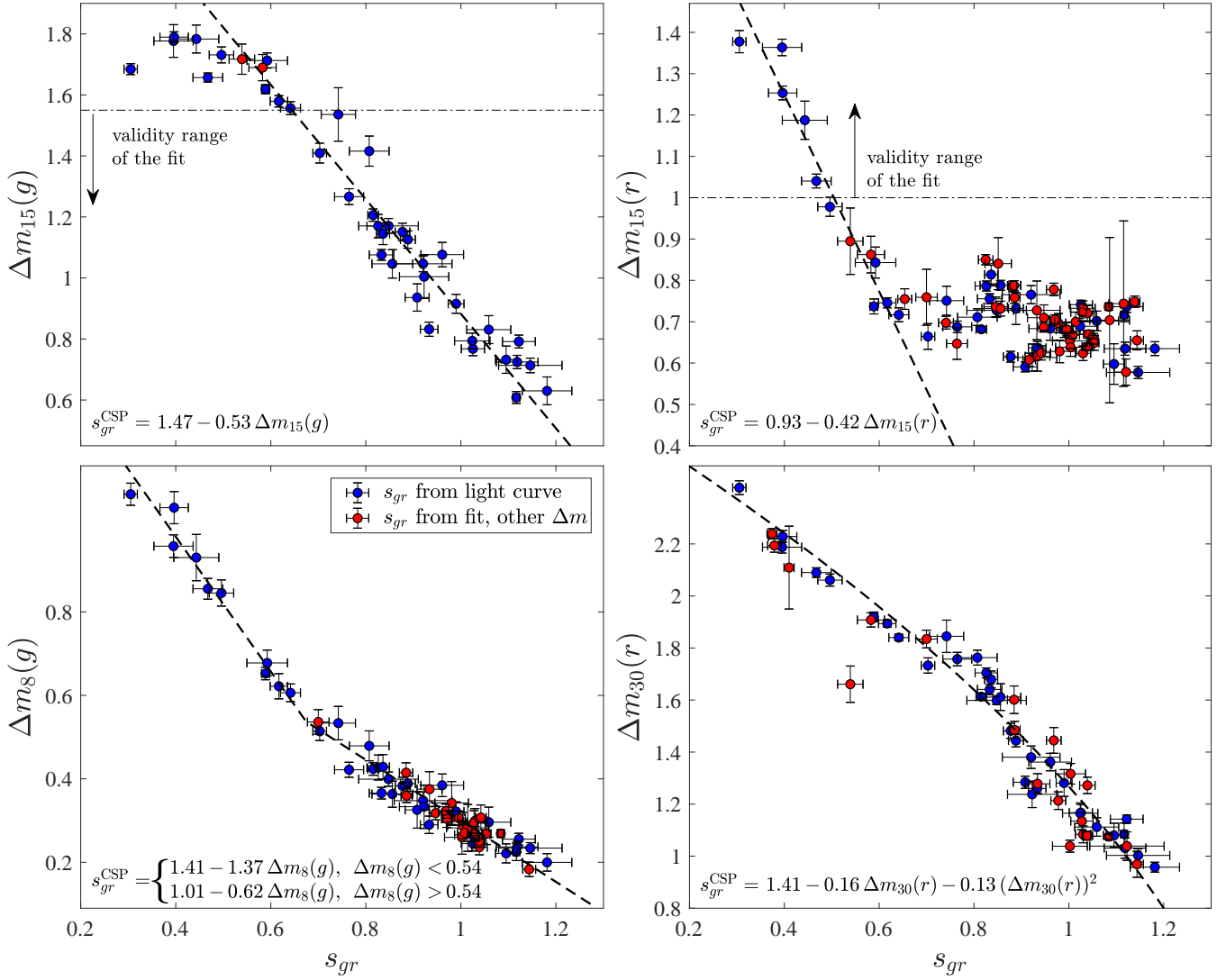


Figure D1. The CSP decline rate parameters as a function of s_{gr} . SNe with a direct s_{gr} measurement are indicated by blue symbols, and SNe whose s_{gr} that was determined using a different decline rate parameter are marked by red symbols. Also shown are the fits of the decline rate (black dashed lines) and the validity range of the $\Delta m_{15}(g)$ and $\Delta m_{15}(r)$ fits.

Table D1. CSP sample g - and r -band color stretches, decline rates and luminosity parameters. The complete table is available in the electronic supplementary material.

name	s_{gr}	s_{gr} src ^a	$\Delta m_{15}(g)$	$\Delta m_{15}(r)$	$\Delta m_8(g)$	$\Delta m_{30}(r)$	M_g	M_r	$M_{Ni56}[M_\odot]$
2004ef	0.82 ± 0.01	dir	1.21 ± 0.02	0.68 ± 0.01	0.42 ± 0.02	1.61 ± 0.01	-19.17 ± 0.00	-19.10 ± 0.00	–
2004eo	0.88 ± 0.02	dir	1.15 ± 0.03	0.62 ± 0.01	0.38 ± 0.02	1.48 ± 0.03	-19.12 ± 0.01	-19.00 ± 0.00	0.47 ± 0.12
2004ey	1.12 ± 0.03	dir	0.79 ± 0.02	0.74 ± 0.01	0.26 ± 0.01	1.14 ± 0.02	-19.44 ± 0.00	-19.27 ± 0.00	–
2004gc	0.92 ± 0.01	$\Delta m_{30}(r)$	–	0.61 ± 0.02	–	1.43 ± 0.02	–	-19.01 ± 0.00	–
2004gs	0.70 ± 0.01	dir	1.41 ± 0.03	0.66 ± 0.03	0.51 ± 0.02	1.73 ± 0.03	-18.96 ± 0.00	-18.87 ± 0.01	0.40 ± 0.08
2004gu	1.05 ± 0.06	$\Delta m_8(g)$	0.88 ± 0.07	0.65 ± 0.02	0.26 ± 0.04	1.04 ± 0.02	-19.45 ± 0.01	-19.48 ± 0.01	–
2005ag	1.02 ± 0.04	$\Delta m_8(g)$	0.88 ± 0.06	0.64 ± 0.02	0.29 ± 0.03	1.32 ± 0.04	-19.53 ± 0.01	-19.46 ± 0.01	–
2005al	0.82 ± 0.02	$\Delta m_{30}(r)$	–	0.85 ± 0.01	–	1.60 ± 0.03	–	-19.12 ± 0.00	–
2005am	0.74 ± 0.02	$\Delta m_{30}(r)$	–	0.70 ± 0.02	–	1.74 ± 0.03	–	-18.90 ± 0.01	–
2005A	0.91 ± 0.03	dir	0.94 ± 0.04	0.59 ± 0.01	0.33 ± 0.04	1.28 ± 0.02	-19.27 ± 0.01	-19.36 ± 0.01	–
2005bg	–	none	–	0.79 ± 0.12	–	–	–	-18.51 ± 0.04	–
2005bl	0.43 ± 0.02	$\Delta m_8(g)$	–	–	0.94 ± 0.03	–	-17.69 ± 0.01	-17.99 ± 0.02	–
2005bo	0.85 ± 0.03	$\Delta m_{30}(r)$	–	0.84 ± 0.06	–	1.55 ± 0.05	–	-19.11 ± 0.01	–
2005eq	1.18 ± 0.05	dir	0.63 ± 0.05	0.63 ± 0.02	0.20 ± 0.02	0.96 ± 0.02	-19.54 ± 0.01	-19.37 ± 0.01	0.84 ± 0.24
2005hc	1.04 ± 0.02	$\Delta m_8(g)$	0.83 ± 0.03	0.62 ± 0.02	0.27 ± 0.02	1.08 ± 0.03	-19.57 ± 0.01	-19.42 ± 0.00	0.70 ± 0.16
2005hj	1.10 ± 0.02	dir	0.73 ± 0.04	0.60 ± 0.05	0.22 ± 0.02	1.08 ± 0.05	-19.51 ± 0.01	-19.44 ± 0.01	–
2005iq	0.92 ± 0.02	$\Delta m_8(g)$	1.10 ± 0.02	0.76 ± 0.01	0.36 ± 0.02	1.49 ± 0.03	-19.33 ± 0.01	-19.13 ± 0.01	–
2005ir	1.02 ± 0.08	$\Delta m_8(g)$	0.86 ± 0.08	0.70 ± 0.02	0.28 ± 0.06	–	-19.52 ± 0.01	-19.47 ± 0.01	–
2005kc	0.97 ± 0.02	$\Delta m_8(g)$	0.98 ± 0.02	0.69 ± 0.01	0.32 ± 0.02	–	-19.28 ± 0.00	-19.11 ± 0.00	–
2005ke	0.47 ± 0.03	dir	1.66 ± 0.01	1.04 ± 0.02	0.86 ± 0.02	2.09 ± 0.02	-17.85 ± 0.01	-18.15 ± 0.01	0.13 ± 0.03

^a The source for the s_{gr} value. The options are either 'dir' (directly from the light curve) or one of the decline rates.**Table D2.** CSP sample B - and V -band color stretches, decline rates and luminosity parameters. The complete table is available in the electronic supplementary material.

name	s_{BV}	$\Delta m_{15}(B)$	$\Delta m_{15}(V)$	$\Delta m_8(B)$	$\Delta m_{30}(V)$	M_B	M_V	$M_{Ni56}[M_\odot]$
2004ef	0.83 ± 0.03	1.41 ± 0.03	0.84 ± 0.02	0.49 ± 0.02	1.98 ± 0.02	-19.13 ± 0.00	-19.07 ± 0.00	–
2004eo	0.84 ± 0.02	1.43 ± 0.03	0.82 ± 0.04	0.52 ± 0.02	1.87 ± 0.03	-19.07 ± 0.00	-18.98 ± 0.01	0.47 ± 0.12
2004ey	1.16 ± 0.04	0.94 ± 0.10	–	0.31 ± 0.02	1.52 ± 0.02	-19.42 ± 0.00	-19.33 ± 0.00	–
2004gs	0.74 ± 0.02	1.64 ± 0.04	1.02 ± 0.03	0.65 ± 0.02	2.13 ± 0.03	-18.90 ± 0.01	-18.87 ± 0.01	0.40 ± 0.08
2004gu	–	–	0.55 ± 0.07	–	1.36 ± 0.06	–	-19.41 ± 0.01	–
2005ag	–	–	0.58 ± 0.07	–	1.72 ± 0.06	–	-19.47 ± 0.01	–
2005al	–	–	0.79 ± 0.02	–	1.87 ± 0.03	–	-19.16 ± 0.00	–
2005am	–	–	0.85 ± 0.04	–	2.00 ± 0.02	–	-18.90 ± 0.00	–
2005A	–	1.15 ± 0.05	0.73 ± 0.02	0.35 ± 0.04	1.65 ± 0.03	-19.37 ± 0.01	-19.27 ± 0.01	–
2005bl	–	–	–	1.03 ± 0.04	–	-17.43 ± 0.01	-17.87 ± 0.01	–
2005bo	–	–	0.81 ± 0.06	–	1.85 ± 0.07	–	-19.11 ± 0.01	–
2005el	0.84 ± 0.16	1.31 ± 0.14	0.95 ± 0.06	0.44 ± 0.11	2.05 ± 0.05	-19.19 ± 0.03	-19.25 ± 0.04	0.50 ± 0.20
2005eq	1.19 ± 0.09	0.77 ± 0.08	0.55 ± 0.05	0.22 ± 0.04	1.34 ± 0.04	-19.52 ± 0.02	-19.41 ± 0.01	0.84 ± 0.24
2005hc	1.15 ± 0.06	0.96 ± 0.05	0.57 ± 0.02	0.32 ± 0.03	1.46 ± 0.03	-19.50 ± 0.01	-19.43 ± 0.01	0.70 ± 0.16
2005hj	–	0.76 ± 0.06	0.50 ± 0.04	0.31 ± 0.03	1.36 ± 0.03	-19.38 ± 0.01	-19.41 ± 0.01	–
2005iq	0.87 ± 0.08	1.29 ± 0.04	0.82 ± 0.02	0.46 ± 0.03	1.91 ± 0.03	-19.25 ± 0.01	-19.18 ± 0.01	–
2005ir	–	0.95 ± 0.09	0.78 ± 0.04	0.31 ± 0.06	1.91 ± 0.06	-19.49 ± 0.01	-19.55 ± 0.02	–
2005kc	–	1.24 ± 0.04	0.74 ± 0.02	0.39 ± 0.03	–	-19.33 ± 0.00	-19.13 ± 0.01	–
2005ke	0.46 ± 0.01	1.77 ± 0.02	1.28 ± 0.02	0.91 ± 0.03	2.14 ± 0.02	-17.56 ± 0.01	-18.04 ± 0.01	0.13 ± 0.03
2005ki	0.87 ± 0.03	1.27 ± 0.04	0.82 ± 0.02	0.39 ± 0.03	1.95 ± 0.02	-19.14 ± 0.01	-19.10 ± 0.01	0.46 ± 0.06

Table D3. BTS sample g - and r -band color stretches and decline rates. The complete table is available in the electronic supplementary material.

name	s_{gr}	s_{gr} src ^a	$\Delta m_{15}(g)$	$\Delta m_{15}(r)$	$\Delta m_8(g)$	$\Delta m_{30}(r)$	dist ^b	LF flag ^c	hostabs ^d	hostcol ^e
2018bpd	1.06 ± 0.06	dm30r	—	0.80 ± 0.04	—	1.13 ± 0.06	160.84	0	-18.60	0.49
2018bxo	1.04 ± 0.06	dm15g	0.97 ± 0.06	0.65 ± 0.09	0.35 ± 0.04	1.13 ± 0.13	278.14	0	-20.86	0.58
2018ccj	0.72 ± 0.07	dm15g	1.50 ± 0.09	—	0.62 ± 0.09	—	—	0	-22.20	1.11
2018ccl	0.90 ± 0.07	dir	1.28 ± 0.07	—	0.50 ± 0.05	1.56 ± 0.04	117.39	0	-22.33	1.19
2018cdt	0.79 ± 0.08	dm15g	1.39 ± 0.10	0.78 ± 0.04	0.50 ± 0.09	—	161.80	0	-22.12	1.15
2018cdu	0.88 ± 0.09	dm15g	1.22 ± 0.13	0.78 ± 0.07	0.44 ± 0.07	—	356.93	0	-22.64	1.13
2018cfa	0.88 ± 0.07	dm15g	1.23 ± 0.08	0.77 ± 0.04	0.41 ± 0.08	1.52 ± 0.08	147.88	0	-18.48	0.89
2018cng	1.09 ± 0.09	dm30r	—	0.70 ± 0.07	—	1.06 ± 0.16	—	0	-17.83	0.96
2018cnw	1.09 ± 0.12	dir	0.76 ± 0.05	0.70 ± 0.10	0.26 ± 0.03	0.99 ± 0.09	97.27	0	-22.61	1.21
2018cny	0.99 ± 0.17	dm15g	1.05 ± 0.28	0.64 ± 0.08	0.35 ± 0.16	1.18 ± 0.08	212.98	0	-21.65	1.26
2018cod	1.24 ± 0.09	dm15g	0.63 ± 0.12	0.64 ± 0.14	0.27 ± 0.04	0.99 ± 0.05	209.20	0	-13.49	0.17
2018coi	0.89 ± 0.12	dm15g	1.21 ± 0.18	0.67 ± 0.09	0.39 ± 0.20	1.59 ± 0.20	266.01	0	-22.48	0.88
2018cri	0.93 ± 0.10	dm15g	1.15 ± 0.14	0.75 ± 0.08	0.38 ± 0.07	1.61 ± 0.14	313.35	0	-17.16	2.49
2018crk	1.11 ± 0.07	dm15g	0.84 ± 0.09	0.30 ± 0.12	0.30 ± 0.06	0.87 ± 0.09	277.45	0	-21.36	1.11
2018crn	0.96 ± 0.15	dm15g	1.10 ± 0.25	0.68 ± 0.10	0.32 ± 0.15	1.37 ± 0.12	266.12	0	-19.38	1.23
2018ctm	1.07 ± 0.08	dm15g	0.91 ± 0.11	0.67 ± 0.11	0.39 ± 0.05	1.28 ± 0.20	307.82	0	-21.23	0.67
2018cto	0.89 ± 0.07	dm30r	1.62 ± 0.22	0.70 ± 0.12	—	1.51 ± 0.08	221.98	0	-22.07	1.17
2018cuw	1.07 ± 0.06	dir	0.91 ± 0.07	0.75 ± 0.07	0.36 ± 0.05	1.14 ± 0.11	129.67	0	-19.40	0.71
2018cvd	0.88 ± 0.10	dm15g	1.24 ± 0.15	—	0.53 ± 0.09	—	385.81	0	-15.17	1.05
2018cvq	0.93 ± 0.14	dm15g	1.14 ± 0.23	0.74 ± 0.12	0.42 ± 0.19	1.21 ± 0.11	300.37	0	-22.12	0.88

^a The source for the s_{gr} value. The options are either 'dir' (directly from the light curve) or one of the decline rates.^b The distance to the SNe in Mpc, calculated from the spectroscopic redshift, if available. If not, it is estimated from the peak magnitudes absolute and observed magnitudes. SNe without s_{gr} or without observed peak magnitudes in both bands do not have an estimated distance.^c A flag indicating if the SN is within the time range of the LF.^d Host galaxy absolute i band magnitude.^e Host galaxy $g - i$ color.**Table D4.** LOSS sample B and V band color stretch, decline rates, and distances. The complete is available in the electronic supplementary material.

name	s_{BV}	s_{BV} src ^a	$\Delta m_{15}(B)$	$\Delta m_{15}(V)$	$\Delta m_8(B)$	$\Delta m_{30}(V)$	dist [Mpc] ^b
1998de	0.46 ± 0.04	$\Delta m_8(B)$	1.87 ± 0.08	1.31 ± 0.03	0.99 ± 0.06	2.28 ± 0.12	69.20
1998dh	0.93 ± 0.06	dir	1.17 ± 0.02	0.72 ± 0.04	0.40 ± 0.02	1.66 ± 0.07	37.00
1998dk	—	none	—	—	—	—	53.80
1998dm	1.18 ± 0.09	dir	0.81 ± 0.05	0.64 ± 0.05	0.28 ± 0.03	1.36 ± 0.06	25.80
1998ef	0.96 ± 0.05	dir	1.18 ± 0.02	0.71 ± 0.02	0.44 ± 0.03	1.77 ± 0.06	74.20
1998es	1.09 ± 0.04	$\Delta m_8(B)$	0.87 ± 0.07	0.48 ± 0.04	0.28 ± 0.04	1.25 ± 0.07	43.00
1999aa	1.21 ± 0.06	dir	0.83 ± 0.09	0.61 ± 0.06	0.24 ± 0.05	1.31 ± 0.07	60.10
1999ac	0.93 ± 0.07	dir	1.23 ± 0.04	0.80 ± 0.04	0.40 ± 0.04	1.58 ± 0.03	40.70
1999bh	—	none	—	—	—	—	74.00
1999by	0.49 ± 0.02	dir	1.91 ± 0.02	1.29 ± 0.02	1.01 ± 0.02	2.17 ± 0.02	11.40
1999cl	0.93 ± 0.10	dir	1.08 ± 0.03	0.72 ± 0.03	0.38 ± 0.02	1.62 ± 0.05	13.10
1999cp	0.97 ± 0.02	$\Delta m_8(B)$	1.02 ± 0.02	0.69 ± 0.02	0.38 ± 0.02	1.51 ± 0.02	39.40
1999da	0.48 ± 0.03	$\Delta m_8(B)$	1.93 ± 0.06	1.29 ± 0.03	0.96 ± 0.05	2.18 ± 0.06	54.30
1999dk	0.99 ± 0.09	dir	1.12 ± 0.04	0.82 ± 0.03	0.36 ± 0.04	1.77 ± 0.07	61.70
1999dq	1.17 ± 0.13	dir	0.81 ± 0.05	0.62 ± 0.08	0.22 ± 0.04	1.42 ± 0.06	59.40
1999ej	0.81 ± 0.02	$\Delta m_8(B)$	1.52 ± 0.03	0.86 ± 0.03	0.54 ± 0.02	1.99 ± 0.03	57.80
1999ek	0.93 ± 0.02	$\Delta m_8(B)$	1.23 ± 0.03	0.70 ± 0.03	0.42 ± 0.02	1.61 ± 0.06	72.00
1999gd	—	none	—	—	—	—	77.00
2000dm	0.88 ± 0.08	dir	1.50 ± 0.05	0.86 ± 0.03	0.50 ± 0.03	2.01 ± 0.05	64.20
2000dr	0.81 ± 0.08	dir	1.73 ± 0.10	1.02 ± 0.03	0.66 ± 0.06	2.13 ± 0.06	75.60

^a The source for the s_{BV} value. The options are either 'dir' (directly from the light curve) or one of the decline rates.^b Distance to the host galaxy, as given in Li et al. (2011a).